ROYAL SOCIETY OPEN SCIENCE

royalsocietypublishing.org/journal/rsos

Research

Cite this article: Girelli A, Giantesio G, Musesti A, Penta R. 2024 Multiscale homogenization for dual porosity time-dependent Darcy–Brinkman/Darcy coupling and its application to the lymph node. *R. Soc. Open Sci.* **11**: 231983. https://doi.org/10.1098/rsos.231983

Received: 10 January 2024
Accepted: 17 April 2024

Subject Category:
Mathematics

Subject Areas:
applied mathematics/differential equations/mathematical modelling

Keywords:
mathematics, lymph node, multiscale, time-dependent, homogenization, Darcy–Brinkman

Author for correspondence:
R. Penta
e-mail: Raimondo.Penta@glasgow.ac.uk

Multiscale homogenization for dual porosity time-dependent Darcy–Brinkman/Darcy coupling and its application to the lymph node

A. Girelli[1], G. Giantesio[1,2], A. Musesti[1] and R. Penta[3]

[1]Dipartimento di Matematica e Fisica 'N. Tartaglia', Università Cattolica del Sacro Cuore, Brescia, Italy
[2]'Mathematics for Technology, Medicine and Biosciences', Università degli Studi di Ferrara, Ferrara, Italy
[3]School of Mathematics and Statistics, University of Glasgow, Glasgow, UK

AG, 0000-0003-3581-7726; GG, 0000-0002-7303-7408; AM, 0000-0003-0965-3991; RP, 0000-0003-1202-8775

We study the coupling between time-dependent Darcy–Brinkman and the Darcy equations at the *microscale* subjected to inhomogeneous body forces and initial conditions to describe a double porosity problem. We derive the homogenized governing equations for this problem using the asymptotic homogenization technique, and as macroscopic results, we obtain a coupling between two Darcy equations, one of which with memory effects, with mass exchange between phases. The memory effects are a consequence of considering the time dependence in the Darcy–Brinkman equation, and they allow us to study in more detail the role of time in the problem under consideration. After the formulation of the model, we solve it in a simplified setting and we use it to describe the movement of fluid within a vascularized lymph node.

1. Introduction

The flow of fluids through porous media is a fundamental process with wide-ranging applications in various fields, such as hydrogeology and biology. In particular, porous media with dual porosity, where fluid flow occurs in different compartments with different pore structures, have garnered growing attention because of their widespread occurrence in both natural and engineered environments [1–7].

THE ROYAL SOCIETY PUBLISHING

In this work, we present a multiscale model for dual-porosity porous media using the *asymptotic homogenization technique* [8,9] that couples a time-dependent Darcy–Brinkman equation [10] with a Darcy equation [8,9,11,12] which describes the fluid flow of the blood vessels inside the node, as our starting point. Here, we assume that the Darcy equation depends on time only parametrically. The theoretical justification of the Darcy–Brinkman equation is less warranted from a multiscale perspective compared to the Darcy equation [8,13–19]; however, since its structure is halfway between the Darcy and the Stokes equations, it can serve as a valid starting point for a multiscale formulation [1], and grants the ability to specify boundary conditions in more detail [20,21]. Moreover, the Darcy–Brinkman equation is also well defined in a time-dependent setting [14,22,23].

We consider a multiscale volume load that drives the coarse scale fluid flow acting on both the Darcy and Darcy–Brinkman problems [24]. These forces can occur from the use of electromagnetic fields, in magnetorheological fluids and in electrolytes that permeate non-uniform tissues [24]. Moreover, we consider a multiscale initial condition of the time-dependent problem that we take into account. Such initial conditions can arise for the flow of fluids in porous media with drug injection [25] or when as an initial condition we have another multiscale motion.

The derived model comprises porous media flow with memory effects (e.g. [8,26–29]), which are encoded in the effective hydraulic conductivity; thus, the nature of the obtained differential problem is intrinsically different with respect to [1]. The latter is represented by a convolution in time between the time-dependent hydraulic conductivity (obtained by solving the differential problem at the cell level) and the macroscopic pressure gradient. The macroscopic Darcy equation with memory effect that we obtain is new and differs from previous works on this subject such as [8,26–29] because we consider the effect of inhomogeneous body forces, a multiscale initial condition and the fluid exchange with another phase (described here by the Darcy equation). Using asymptotic homogenization, we pass from an equation at the microscale where *the present time is necessary for deducing the future* [30] to a macroscopic equation where *the present and the past are necessary to deduce the future* [31]. The memory effects appear to be a natural framework when dealing with the homogenization of this kind of problems [30,31].

Among the countless applications of dual-porosity porous media, the main motivation that guided us to propose and study this model is the application of the latter to the fluid flow of a lymph node, an essential part of the lymphatic system. The lymphatic system is composed of a network of vessels, capillaries and organs [32]. The interstitial fluid is drained by the *lymphatic capillaries* and it is called *lymph* once inside the lymphatic system. Inside the lymphatic vessels, there is a series of *one-way valves* which prevent retrograde flows. The part of the vessel between two valves is called *lymphangion*. Lymphangion walls are innervated with sympathetic and parasympathetic nerves [33–35] and can perform rhythmic contractions, making lymph transport a time-dependent flow [33,36–38]. The lymphatic system is an integral part of the immune system thanks to the *lymph nodes*. The lymph node is vital for immune defence, housing B and T cells that circulate in the body to protect against infection. B cells generate antibodies to fight antigens, while stimulated B cells transform into plasma or memory cells. Antigen-presenting cells capture antigens and present them to T cells in the lymph nodes, activating the adaptive immune response. Lymph transport has an important function in transporting immune cells, proteins, cancer metastasis, drugs and so on [39–41]. Furthermore, the movement of fluid through lymph nodes promotes the expression of chemokines, establishing a chemokine gradient that directs the movement of immune cells into the node. Changes in lymph transport play an important role in several pathologies. Elevated fluid flow augments the growth rate and sensitivity to drugs in specific forms of lymphomas [42]. Inadequate lymph transport can lead to a condition called lymphœdema, where excess interstitial fluid accumulates in the tissues, and it is often caused due to an impairment of lymph nodes [36,43]. From a mechanical perspective, the key characteristics of the lymph node include the lymphoid compartment (LC), which is a porous bulk region and forms the parenchyma of the lymph node, and the subcapsular sinus (SCS), a thin channel near the wall that surround the LC and that allows free-fluid flow [33]. The fluid can enter the LC from the SCS through a conduit system network created by fibroblastic reticular cells (FRCs) [44–46] which forms the main porous region of the lymph node. The lymph node is a highly vascularized organ, and inside the LC there are plenty of blood vessels that allow fluid and substance exchange [47–49], making the lymph node an important connection region between the lymphatic system and the blood system.

To the best of our knowledge, only a few models in the literature try to describe the fluid dynamical aspects of lymph node behaviour [50–52]. In [53,54], it is explored how the fluid flow in the lymph node is influenced by its internal structure, using an image-based model to establish a relationship between the greyscale values of the images and the permeability of the lymph node tissue, using this as the

permeability for the steady Darcy equation. In [47], the authors conduct a parameter sensitivity analysis by using a computational flow model based on a mouse popliteal lymph node, coupling a steady Darcy–Brinkman equation in the LC with a steady Navier–Stokes equation in the SCS. Grebennikov and others [45,46] study the lymph flow through the conduit system network using an object-oriented computational algorithm to generate the three-dimensional geometry of the FRC graph network. In [55], the fluid flow within the lymph node is simulated by using a microfluidic device that mimics the microenvironment of a lymph node. Birmingham *et al*. [39] focused on the lymph node's SCS fluid dynamics thanks to a microfluidic platform, evaluating how physiological flow patterns impact the adhesion of metastatic cancer cells (thanks to the wall shear stress values). In [56], a numerical method is developed to simulate the fluid flow in the lymph node using boundary integral equations, and then in [57] the authors provide an artificial neural network model to describe the lymph node drainage function. In [1,58,59], we have the first explicit models that describe the fluid flow in the lymph node in simplified geometries. In particular, in [58,59], they found a divergence-free explicit and numerical solution in a time-dependent setting, with a very idealized geometry for [58] and a spherical geometry in [59]. Girelli *et al*. [1] describe the blood vessel drainage function in the lymph node considering the multiscale nature of the latter in a steady setting, obtaining a rigorous mathematical model using the asymptotic homogenization technique; thanks to this approach, they were able to describe the fluid flow inside the conduit system network (formed by FRC) and inside the blood vessels networks.

This work addresses a crucial limitation characterizing the work in [1], as it takes into account the time-dependent character of the pulsatile flow which takes place in the lymph node due to the pulsation of the lymphangions [36,60,61] and its upscaling onto the macroscale. In fact, we present a multiscale model using the *asymptotic homogenization technique* [8,9] that couples a time-dependent Darcy–Brinkman equation [10], which describes the fluid flow inside the conduit system network formed by FRC, with a Darcy equation [8,9,11,12], which describes the fluid flow of the blood vessels inside the node, as our starting point. The Darcy equation depends on time only parametrically because the time-dependency we take into account is given by the lymphangion pulsation and affects mainly the lymph flow inside the FRC network. This model focuses on the porous region of the lymph node (LC) and the fluid exchange occurring solely between the node and the blood vessels within this specific area [47–49]. It is crucial to emphasize that, as highlighted in [1], our analysis begins with the Darcy–Brinkman and Darcy equations. This implies that variations in pore-scale geometry have been effectively averaged out, eliminating the necessity for precise details about the intricate and challenging-to-describe microstructure geometry of the lymph node.

In §2, we show the starting equations and boundary conditions of our problem, based on the balance equations of continuum mechanics. In §3, we employ the asymptotic homogenization technique and in §4, we find the macroscopic averaged equations. In §5, we find the explicit solution to our problem in spherical geometry under the hypothesis of axisymmetry with respect to the azimuthal angle and isotropy of the porous medium using the Fourier transform and using the explicit solution that we already found in [1]. In §6, we describe the numerical simulation that we use to solve the problem in the cell domain. Finally, in §7, we solve the explicit solution we found in §5 using lymph node physiological data obtained from the literature, allowing us to study in more detail the behaviour of the lymph inside the lymph node in a time-dependent setting.

2. Formulation of the starting problem

We consider the domain $\Omega = \Omega_v \cup \Omega_m$, where Ω_m and Ω_v denote regions of the matrix and the vessels, respectively. A sketch of a portion of the three-dimensional domain at hand comprising the two phases is provided in figure 1. We describe the fluid flow in Ω_v via Darcy's Law supplemented by a body force as in the work [24], namely

$$\begin{cases} \boldsymbol{v}_v(\boldsymbol{x}, t) = -\tilde{K}_v(\boldsymbol{x})(\nabla p_v(\boldsymbol{x}, t) - \boldsymbol{b}_v(\boldsymbol{x}, t)) & \text{in } \Omega_v \times [0, T] \\ \nabla \cdot \boldsymbol{v}_v(\boldsymbol{x}, t) = 0 & \text{in } \Omega_v \times [0, T]. \end{cases} \tag{2.1}$$

In order to model the unsteady fluid flow within the matrix phase Ω_m, we exploit the following *Darcy–Brinkman* equation [1,10,24]:

$$\begin{cases} \rho_0 \frac{\partial \boldsymbol{v}_m}{\partial t}(\boldsymbol{x}, t) = -\nabla p_m(\boldsymbol{x}, t) - \tilde{K}_m^{-1}(\boldsymbol{x})\boldsymbol{v}_m(\boldsymbol{x}, t) + \mu_e \Delta \boldsymbol{v}_m(\boldsymbol{x}, t) + \boldsymbol{b}_m(\boldsymbol{x}, t) & \text{in } \Omega_m \times [0, T] \\ \nabla \cdot \boldsymbol{v}_m(\boldsymbol{x}, t) = 0 & \text{in } \Omega_m \times [0, T]. \end{cases} \tag{2.2}$$

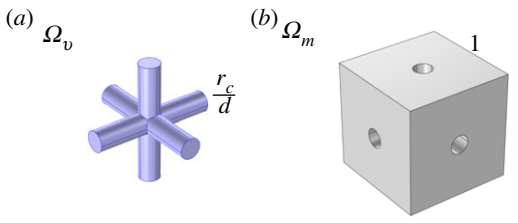

Figure 1. A sketch of a periodic portion of the domain comprising the vessels Ω_v (*a*) and matrix Ω_m (*b*).

For $\gamma = v, m$, $\boldsymbol{v}_\gamma$ is the velocity of the fluid in the region Ω_γ, p_γ is the pressure in the region Ω_γ, $\boldsymbol{b}_\gamma$ is the inhomogeneous external force density in the region Ω_γ, $\tilde{K}_\gamma(\boldsymbol{x})$ is the *hydraulic conductivity tensor* in the region Ω_γ, μ_e is the *effective viscosity*, and ρ_0 is the fluid *density*. For $\gamma = v, m$, we suppose that the hydraulic conductivity tensor is symmetric and positive definite:

$$\tilde{K}_\gamma(\boldsymbol{x}) = \tilde{K}_\gamma^T(\boldsymbol{x}), \quad \forall\, \boldsymbol{a} \neq \boldsymbol{0} : \boldsymbol{a} \cdot \tilde{K}_\gamma(\boldsymbol{x})\boldsymbol{a} > 0. \tag{2.3}$$

Our starting point consists of both Darcy and Darcy–Brinkman equations, assuming that the pore structure is homogenized in both compartments. In this scenario, the hydraulic conductivity tensor $\tilde{K}_\gamma(\boldsymbol{x})$ functions as a means to represent the essential microscale geometric information.

The matrix and the vessels are coupled via the following interface conditions:

$$\begin{cases} \boldsymbol{v}_v(\boldsymbol{x}, t) \cdot \boldsymbol{n} = \boldsymbol{v}_m(\boldsymbol{x}, t) \cdot \boldsymbol{n} = L_p(p_m(\boldsymbol{x}, t) - p_v(\boldsymbol{x}, t) - \bar{p}(t)) & \text{on } \Gamma \times [0, T] \\ \boldsymbol{v}_m(\boldsymbol{x}, t) \cdot \boldsymbol{\tau} = -\frac{\sqrt{\mu \tilde{K}_m(\boldsymbol{x})}}{\alpha} [(\boldsymbol{n} \cdot \nabla)\boldsymbol{v}_m(\boldsymbol{x}, t)] \cdot \boldsymbol{\tau} & \text{on } \Gamma \times [0, T], \end{cases} \tag{2.4}$$

where $\Gamma = \partial\Omega_m \cap \partial\Omega_v$, $\boldsymbol{n}$ is the outer normal to Ω_m, $\boldsymbol{\tau}$ is any tangential vector to Γ, $\bar{p}(t)$ is a function that depends only on time and α is a constant that depends on the physico-chemical properties of the interface. The first interface condition of (2.4) is related to the normal component of the velocity; if we take $\bar{p} = \sigma(\pi_m - \pi_v)$, we obtain the well-known *Starling equation* [62,63], used to describe the fluid exchange between two regions separated by a porous membrane, where σ is the *Staverman reflection coefficient*, π_v the *osmotic pressure of* Ω_v and π_m the *osmotic pressure of* Ω_m. For simplicity, in this work, we assume that the osmotic pressures π_v and π_m depend only on time, but they can depend also on space [3]. The parameter L_p is typically experimentally measured and depends on the geometry and porosity/leakage of the vessels' walls Γ. We consider this particular interface condition because we aim to apply this model to the fluid flow of a lymph node, but our formulation remains valid for other applications too. The second equation of (2.4) is the *Beavers–Joseph–Saffman boundary condition* [64], an interface condition on the tangent component of the velocity introduced in [65,66]. This interface condition introduces a slip velocity, which is proportional to the normal component of the velocity gradient of the fluid near the boundary. This interface condition is often used to describe the connection between free-fluid and porous regions, as well as an interface condition for dual-porosity media [2,67]. Moreover, linking the Darcy–Brinkman equation with the Darcy equation necessitates conditions reliant on the actual velocity. Therefore, the Beavers–Joseph conditions offer a more comprehensive grasp of the underlying physics compared to merely imposing a zero tangent velocity.

The initial condition is

$$\boldsymbol{v}_m(\boldsymbol{x}, 0) = \boldsymbol{v}_{m,0}(\boldsymbol{x}) \quad \text{in } \Omega_m, \tag{2.5}$$

where $\boldsymbol{v}_{m,0}(\boldsymbol{x})$ need to satisfy $\nabla \cdot \boldsymbol{v}_{m,0}(\boldsymbol{x}) = 0$ and must be compatible with the interface conditions (2.4).

The non-dimensional form of the Darcy equation, the Darcy–Brinkman equation, and the interface conditions for the domain Ω_γ, with $\gamma = m, v$, are as follows. We denote with a prime symbol the following non-dimensional quantities:

$$t = \frac{L}{U} t', \quad \boldsymbol{v}_\gamma = U\boldsymbol{u}'_\gamma, \quad \boldsymbol{x} = L\boldsymbol{x}', \quad \tilde{K}_\gamma = K_{\text{ref}} K'_\gamma, \quad \boldsymbol{b}_\gamma = \frac{U}{K_{\text{ref}}} \boldsymbol{b}'_\gamma, \quad p_\gamma = \frac{UL}{K_{\text{ref}}} p'_\gamma \tag{2.6}$$

and

$$\epsilon = \frac{d}{L}, \tag{2.7}$$

where U is the *characteristic velocity*, K_{ref} is the *representative (scalar) hydraulic conductivity*, d is the *fine-scale length* and L is the *coarse-scale length*. In the scope of this work, the parameter d takes on the role of

denoting the separation between two vascularized regions. Instead of delving into the intricate particulars of individual vessels, the vascular network region is conceptualized as a geometric domain denoted as Ω_v, consisting of interconnected cylinders with radius r_c (illustrated in figure 1), where the Darcy equation is applicable. Accordingly, d is precisely characterized as the distance between two neighbouring cylinders within this model representation.

Substituting (2.6) into (2.2), we obtain, by neglecting the primes

$$\begin{cases} \eta \frac{\partial \boldsymbol{v}_m}{\partial t}(\boldsymbol{x}, t) = -\nabla p_m(\boldsymbol{x}, t) - K_m^{-1}(\boldsymbol{x})\boldsymbol{v}_m(\boldsymbol{x}, t) + \tilde{\mu}\Delta \boldsymbol{v}_m(\boldsymbol{x}, t) + \boldsymbol{b}_m(\boldsymbol{x}, t) & \text{in } \Omega_m \times [0, T], \\ \nabla \cdot \boldsymbol{v}_m(\boldsymbol{x}, t) = 0 & \text{in } \Omega_m \times [0, T], \end{cases} \tag{2.8}$$

where

$$\eta = \frac{\rho_0 U K_{\text{ref}}}{L} \quad \text{and} \quad \tilde{\mu} = \frac{K_{\text{ref}} \mu_e}{L^2}.$$

As d represents the fine-scale length in our problem, the most natural choice as a representative fine-scale conductivity, which we denote as K_{ref}, resides, given its physical dimensions, in choosing d^2/μ, i.e.

$$K_{\text{ref}} = \frac{d^2}{\mu}, \quad \eta = \frac{\rho_0 U d^2}{\mu L}, \quad \tilde{\mu} = \epsilon^2 \mu^*, \quad \mu^* = \frac{\mu_e}{\mu}. \tag{2.9}$$

Substituting these relations into (2.1) and (2.8), we obtain the non-dimensional equations

$$\begin{cases} \boldsymbol{v}_v(\boldsymbol{x}, t) = -K_v(\boldsymbol{x})(\nabla p_v(\boldsymbol{x}, t) - \boldsymbol{b}_v(\boldsymbol{x}, t)) & \text{in } \Omega_v \times [0, T] \\ \nabla \cdot \boldsymbol{v}_v(\boldsymbol{x}, t) = 0 & \text{in } \Omega_v \times [0, T] \end{cases} \tag{2.10}$$

and

$$\begin{cases} \eta \frac{\partial \boldsymbol{v}_m}{\partial t}(\boldsymbol{x}, t) = -\nabla p_m(\boldsymbol{x}, t) - K_m^{-1}(\boldsymbol{x})\boldsymbol{v}_m(\boldsymbol{x}, t) + \epsilon^2 \mu^* \Delta \boldsymbol{v}_m(\boldsymbol{x}, t) + \boldsymbol{b}_m(\boldsymbol{x}, t) & \text{in } \Omega_m \times [0, T], \\ \nabla \cdot \boldsymbol{v}_m(\boldsymbol{x}, t) = 0 & \text{in } \Omega_m \times [0, T]. \end{cases} \tag{2.11}$$

We also need to non-dimensionalize the interface conditions (2.4). In particular, we adopt the same distinguished limit embraced in [3, 68] which ensures that the blood flux stays finite when the length-scale separation that exists in the system becomes more and more pronounced. This is equivalent to assuming

$$\begin{cases} \boldsymbol{v}_v(\boldsymbol{x}, t) \cdot \boldsymbol{n} = \boldsymbol{v}_m(\boldsymbol{x}, t) \cdot \boldsymbol{n} = \epsilon \bar{L}_p(p_m(\boldsymbol{x}, t) - p_v(\boldsymbol{x}, t) - \bar{p}(t)) & \text{on } \Gamma \times [0, T] \\ \boldsymbol{v}_m(\boldsymbol{x}, t) \cdot \boldsymbol{\tau} = -\epsilon \frac{\sqrt{K_m(\boldsymbol{x})}}{\alpha}[(\boldsymbol{n} \cdot \nabla)\boldsymbol{v}_m(\boldsymbol{x}, t)] \cdot \boldsymbol{\tau} & \text{on } \Gamma \times [0, T], \end{cases} \tag{2.12}$$

where $\bar{L}_p = L_p \mu L^2/d^3$ [3]. Moreover, we close our problem using periodic boundary conditions at the boundary $\partial\Omega \setminus \Gamma$.

3. The multiscale formulation

The goal of this section is to derive a macroscale model for the continuum system of equations (2.10), (2.5), (2.11) and (2.12), using the asymptotic homogenization technique [8,9,69]. We assume that there is a clear separation between the spatial fine scale d and the coarse scale L, which means that the quantity ϵ defined in (2.7) is small:

$$\epsilon \ll 1.$$

To achieve spatial scale decoupling, we introduce a fresh local variable

$$\boldsymbol{y} = \frac{\boldsymbol{x}}{\epsilon}, \tag{3.1}$$

where $\boldsymbol{x}$ represents the coarse-scale spatial coordinates and $\boldsymbol{y}$ represents the fine-scale spatial coordinates: they have to be considered independent in a formal way. We assume that p_γ, $\boldsymbol{v}_\gamma$, K_γ and $\boldsymbol{b}_\gamma$ (where $\gamma = m, v$) depend on both $\boldsymbol{x}$ and $\boldsymbol{y}$.

We assume two main hypotheses concerning the geometry of the multiscale problem: *local periodicity* and *macroscopic uniformity*. Local periodicity means that p_γ, $\boldsymbol{v}_\gamma$, K_γ and $\boldsymbol{b}_\gamma$ are $\boldsymbol{y}$-periodic. By making this assumption, we are able to focus our study on a restricted portion of the fine-scale domain. Instead, macroscopic uniformity means ignoring geometric variations within the cell structure and inclusions concerning the coarse-scale variable $\boldsymbol{x}$, *i.e.* the microstructure is unique. Then we may consider the

utilization of a single periodic cell, denoted as Ω_γ, for each macroscale point $\boldsymbol{x}$, and

$$\nabla_{\boldsymbol{x}} \cdot \int_{\Omega_\gamma} (\bullet) \mathrm{d}\boldsymbol{y} = \int_{\Omega_\gamma} \nabla_{\boldsymbol{x}} \cdot (\bullet)\, \mathrm{d}\boldsymbol{y}. \tag{3.2}$$

The differential operator becomes

$$\nabla \to \nabla_{\boldsymbol{x}} + \frac{1}{\epsilon} \nabla_{\boldsymbol{y}}; \tag{3.3}$$

we now employ a power series expansion for ϵ for the variables of our problem as follows (where $\gamma = m, v$):

$$\boldsymbol{v}_\gamma(\boldsymbol{x}, \boldsymbol{y}, t) \equiv \boldsymbol{v}_\gamma^\epsilon(\boldsymbol{x}, \boldsymbol{y}, t) = \sum_{l=0}^{\infty} \boldsymbol{v}_\gamma^{(l)}(\boldsymbol{x}, \boldsymbol{y}, t)\epsilon^l, \tag{3.4}$$

$$p_\gamma(\boldsymbol{x}, \boldsymbol{y}, t) \equiv p_\gamma^\epsilon(\boldsymbol{x}, \boldsymbol{y}, t) = \sum_{l=0}^{\infty} p_\gamma^{(l)}(\boldsymbol{x}, \boldsymbol{y}, t)\epsilon^l, \tag{3.5}$$

$$\boldsymbol{b}_\gamma(\boldsymbol{x}, \boldsymbol{y}, t) \equiv \boldsymbol{b}_\gamma^\epsilon(\boldsymbol{x}, \boldsymbol{y}, t) = \sum_{l=0}^{\infty} \boldsymbol{b}_\gamma^{(l)}(\boldsymbol{x}, \boldsymbol{y}, t)\epsilon^l \tag{3.6}$$

and

$$\boldsymbol{v}_{m,0}(\boldsymbol{x}, \boldsymbol{y}) \equiv \boldsymbol{v}_{m,0}^\epsilon(\boldsymbol{x}, \boldsymbol{y}) = \sum_{l=0}^{\infty} \boldsymbol{v}_{m,0}^{(l)}(\boldsymbol{x}, \boldsymbol{y})\epsilon^l. \tag{3.7}$$

Substituting the asymptotic expansions (3.4)–(3.7) and the differential operator (3.3) into equations (2.10)–(2.11), we have

$$\begin{cases} \epsilon \boldsymbol{v}_v^\epsilon(\boldsymbol{x}, \boldsymbol{y}, t) + \epsilon K_v(\boldsymbol{x}, \boldsymbol{y}) \nabla_{\boldsymbol{x}} p_v^\epsilon(\boldsymbol{x}, \boldsymbol{y}, t) \\ \qquad + K_v(\boldsymbol{x}, \boldsymbol{y}) \nabla_{\boldsymbol{y}} p_v^\epsilon(\boldsymbol{x}, \boldsymbol{y}, t) - \epsilon K_v(\boldsymbol{x}, \boldsymbol{y}) \boldsymbol{b}_v^\epsilon(\boldsymbol{x}, \boldsymbol{y}, t) = \boldsymbol{0} & \text{in } \Omega_v \times [0, T] \\ \epsilon \nabla_{\boldsymbol{x}} \cdot \boldsymbol{v}_v^\epsilon(\boldsymbol{x}, \boldsymbol{y}, t) + \nabla_{\boldsymbol{y}} \cdot \boldsymbol{v}_v^\epsilon(\boldsymbol{x}, \boldsymbol{y}, t) = 0 & \text{in } \Omega_v \times [0, T] \end{cases} \tag{3.8}$$

and

$$\begin{cases} \eta\epsilon \frac{\partial \boldsymbol{v}_m^\epsilon}{\partial t}(\boldsymbol{x}, \boldsymbol{y}, t) = -\epsilon \nabla_{\boldsymbol{x}} p_m^\epsilon(\boldsymbol{x}, \boldsymbol{y}, t) - \nabla_{\boldsymbol{y}} p_m^\epsilon(\boldsymbol{x}, \boldsymbol{y}, t) - \epsilon K_m^{-1}(\boldsymbol{x}, \boldsymbol{y}) \boldsymbol{v}_m^\epsilon(\boldsymbol{x}, \boldsymbol{y}, t) \\ \qquad + \mu^* \epsilon^3 \Delta_{\boldsymbol{x}} \boldsymbol{v}_m^\epsilon(\boldsymbol{x}, \boldsymbol{y}, t) + \mu^* \epsilon \Delta_{\boldsymbol{y}} \boldsymbol{v}_m^\epsilon(\boldsymbol{x}, \boldsymbol{y}, t) \\ \qquad + \mu^* \epsilon^2 \nabla_{\boldsymbol{x}} \cdot (\nabla_{\boldsymbol{y}} \boldsymbol{v}_m^\epsilon(\boldsymbol{x}, \boldsymbol{y}, t)) + \mu^* \epsilon^2 \nabla_{\boldsymbol{y}} \cdot (\nabla_{\boldsymbol{x}} \boldsymbol{v}_m^\epsilon(\boldsymbol{x}, \boldsymbol{y}, t)) \\ \qquad + \epsilon \boldsymbol{b}_m^\epsilon(\boldsymbol{x}, \boldsymbol{y}, t) & \text{in } \Omega_m \times [0, T], \\ \epsilon \nabla_{\boldsymbol{x}} \cdot \boldsymbol{v}_m^\epsilon(\boldsymbol{x}, \boldsymbol{y}, t) + \nabla_{\boldsymbol{y}} \cdot \boldsymbol{v}_m^\epsilon(\boldsymbol{x}, \boldsymbol{y}, t) = 0 & \text{in } \Omega_m \times [0, T], \end{cases} \tag{3.9}$$

and if we substitute them into the interface conditions (2.12) and the initial condition (2.5), we obtain

$$\begin{cases} \boldsymbol{v}_v^\epsilon(\boldsymbol{x}, \boldsymbol{y}, t) \cdot \boldsymbol{n} = \boldsymbol{v}_m^\epsilon(\boldsymbol{x}, \boldsymbol{y}, t) \cdot \boldsymbol{n} = \epsilon \bar{L}_p(p_m^\epsilon(\boldsymbol{x}, \boldsymbol{y}, t) - p_v^\epsilon(\boldsymbol{x}, \boldsymbol{y}, t) - \bar{p}(t)) & \text{on } \Gamma \times [0, T] \\ \boldsymbol{v}_m^\epsilon(\boldsymbol{x}, \boldsymbol{y}, t) \cdot \boldsymbol{\tau} = -\epsilon \frac{\sqrt{K_m(\boldsymbol{x}, \boldsymbol{y})}}{\alpha} \left[\left(\boldsymbol{n} \cdot \left(\nabla_{\boldsymbol{x}} + \frac{1}{\epsilon} \nabla_{\boldsymbol{y}} \right) \right) \boldsymbol{v}_m^\epsilon(\boldsymbol{x}, \boldsymbol{y}, t) \right] \cdot \boldsymbol{\tau} & \text{on } \Gamma \times [0, T] \end{cases} \tag{3.10}$$

and

$$\boldsymbol{v}_m^\epsilon(\boldsymbol{x}, \boldsymbol{y}, 0) = \boldsymbol{v}_{m,0}^\epsilon(\boldsymbol{x}, \boldsymbol{y}) \quad \text{in } \Omega_m. \tag{3.11}$$

3.1. Coefficients of order ϵ^0

Collecting the terms of order ϵ^0 from (3.8) to (3.11), we obtain

$$\nabla_{\boldsymbol{y}} p_v^{(0)}(\boldsymbol{x}, \boldsymbol{y}, t) \Rightarrow p_v^{(0)} = p_v^{(0)}(\boldsymbol{x}, t) \quad \text{in } \Omega_v \times [0, T], \tag{3.12}$$

$$\nabla_{\boldsymbol{y}} p_m^{(0)}(\boldsymbol{x}, \boldsymbol{y}, t) \Rightarrow p_m^{(0)} = p_m^{(0)}(\boldsymbol{x}, t) \quad \text{in } \Omega_m \times [0, T], \tag{3.13}$$

$$\nabla_{\boldsymbol{y}} \cdot \boldsymbol{v}_v^{(0)}(\boldsymbol{x}, \boldsymbol{y}, t) = 0 \quad \text{in } \Omega_v \times [0, T], \tag{3.14}$$

$$\nabla_{\boldsymbol{y}} \cdot \boldsymbol{v}_m^{(0)}(\boldsymbol{x}, \boldsymbol{y}, t) = 0 \quad \text{in } \Omega_m \times [0, T], \tag{3.15}$$

$$\boldsymbol{v}_m^{(0)}(\boldsymbol{x}, \boldsymbol{y}, t) \cdot \boldsymbol{n} = \boldsymbol{v}_v^{(0)}(\boldsymbol{x}, \boldsymbol{y}, t) \cdot \boldsymbol{n} = 0 \quad \text{on } \Gamma \times [0, T], \tag{3.16}$$

$$\boldsymbol{v}_m^{(0)}(\boldsymbol{x}, \boldsymbol{y}, t) \cdot \boldsymbol{\tau} = -\frac{\sqrt{K_m(\boldsymbol{x}, \boldsymbol{y})}}{\alpha} \left[(\boldsymbol{n} \cdot \nabla_{\boldsymbol{y}}) \boldsymbol{v}_m^{(0)}(\boldsymbol{x}, \boldsymbol{y}, t) \right] \cdot \boldsymbol{\tau} \quad \text{on } \Gamma \times [0, T] \tag{3.17}$$

and

$$\boldsymbol{v}_m^{(0)}(\boldsymbol{x}, \boldsymbol{y}, 0) = \boldsymbol{v}_{m,0}^{(0)}(\boldsymbol{x}, \boldsymbol{y}) \quad \text{in } \Omega_m. \tag{3.18}$$

3.2. Coefficients of order ϵ^1

If we collect the terms of order ϵ^1 from equations (3.8) to (3.11), we have

$$\boldsymbol{v}_v^{(0)}(\boldsymbol{x},\boldsymbol{y},t)+K_v(\boldsymbol{x},\boldsymbol{y})\Big(\nabla_x p_v^{(0)}(\boldsymbol{x},t)+\nabla_y p_v^{(1)}(\boldsymbol{x},\boldsymbol{y},t)-\boldsymbol{b}_v^{(0)}(\boldsymbol{x},\boldsymbol{y},t)\Big)=\boldsymbol{0}\quad \text{in } \Omega_v\times[0,T], \tag{3.19}$$

$$\nabla_x\cdot\boldsymbol{v}_v^{(0)}(\boldsymbol{x},\boldsymbol{y},t)+\nabla_y\cdot\boldsymbol{v}_v^{(1)}(\boldsymbol{x},\boldsymbol{y},t)=0\quad \text{in } \Omega_v\times[0,T], \tag{3.20}$$

$$\begin{aligned}\eta\frac{\partial\boldsymbol{v}_m^{(0)}}{\partial t}(\boldsymbol{x},\boldsymbol{y},t)&=-\nabla_x p_m^{(0)}(\boldsymbol{x},t)-\nabla_y p_m^{(1)}(\boldsymbol{x},\boldsymbol{y},t)-K_m^{-1}(\boldsymbol{x},\boldsymbol{y})\boldsymbol{v}_m^{(0)}(\boldsymbol{x},\boldsymbol{y},t)\\&\quad+\mu^*\Delta_y\boldsymbol{v}_m^{(0)}(\boldsymbol{x},\boldsymbol{y},t)+\boldsymbol{b}_m^{(0)}(\boldsymbol{x},\boldsymbol{y},t)\quad \text{on } \Omega_m\times[0,T],\end{aligned} \tag{3.21}$$

$$\nabla_x\cdot\boldsymbol{v}_m^{(0)}(\boldsymbol{x},\boldsymbol{y},t)+\nabla_y\cdot\boldsymbol{v}_m^{(1)}(\boldsymbol{x},\boldsymbol{y},t)=0\quad \text{on } \Omega_m\times[0,T], \tag{3.22}$$

$$\boldsymbol{v}_m^{(1)}(\boldsymbol{x},\boldsymbol{y},t)\cdot\boldsymbol{n}=\boldsymbol{v}_v^{(1)}(\boldsymbol{x},\boldsymbol{y},t)\cdot\boldsymbol{n}=\bar{L}_p(p_m^{(0)}(\boldsymbol{x},t)-p_v^{(0)}(\boldsymbol{x},t)-\bar{p}(t))\quad \text{on } \Gamma\times[0,T], \tag{3.23}$$

$$\boldsymbol{v}_m^{(1)}(\boldsymbol{x},\boldsymbol{y},t)\cdot\boldsymbol{\tau}=-\frac{\sqrt{K_m(\boldsymbol{x},\boldsymbol{y})}}{\alpha}\left[(\boldsymbol{n}\cdot\nabla_x)\boldsymbol{v}_m^{(0)}(\boldsymbol{x},\boldsymbol{y},t)+(\boldsymbol{n}\cdot\nabla_y)\boldsymbol{v}_m^{(1)}(\boldsymbol{x},\boldsymbol{y},t)\right]\cdot\boldsymbol{\tau}\quad \text{on } \Gamma\times[0,T] \tag{3.24}$$

and

$$\boldsymbol{v}_m^{(1)}(\boldsymbol{x},\boldsymbol{y},0)=\boldsymbol{v}_{m,0}^{(1)}(\boldsymbol{x},\boldsymbol{y})\quad \text{in } \Omega_m. \tag{3.25}$$

3.3. Derivation of Darcy's equation

Applying the $\nabla_y\cdot$ operator to (3.19) and remembering equation (3.14), we obtain

$$\nabla_y\cdot[K_v(\boldsymbol{x},\boldsymbol{y})(\nabla_x p_v^{(0)}(\boldsymbol{x},t)+\nabla_y p_v^{(1)}(\boldsymbol{x},\boldsymbol{y},t)-\boldsymbol{b}_v^{(0)}(\boldsymbol{x},\boldsymbol{y},t))]=0\quad \text{in } \Omega_v\times[0,T]; \tag{3.26}$$

it follows that the boundary condition (3.16) is

$$[K_v(\boldsymbol{x},\boldsymbol{y})(\nabla_x p_v^{(0)}(\boldsymbol{x},t)+\nabla_y p_v^{(1)}(\boldsymbol{x},\boldsymbol{y},t)-\boldsymbol{b}_v^{(0)}(\boldsymbol{x},\boldsymbol{y},t))]\cdot\boldsymbol{n}=0\quad \text{on } \Gamma\times[0,T]. \tag{3.27}$$

We note that the problem is linear and that $\nabla_x p_v^{(0)}$ is constant in $\boldsymbol{y}$; hence we formulate the following solution ansatz:

$$p_v^{(1)}(\boldsymbol{x},\boldsymbol{y},t)=\boldsymbol{h}_v(\boldsymbol{x},\boldsymbol{y},t)\cdot\nabla_x p_v^{(0)}(\boldsymbol{x},t)+\tilde{h}_v(\boldsymbol{x},\boldsymbol{y},t). \tag{3.28}$$

The ansatz (3.28) solves the problem (3.26)–(3.27) (it is a solution up to a $\boldsymbol{y}$-constant function), provided that the auxiliary vector and scalar fields $\boldsymbol{h}_v$ and $\tilde{h}_v$ solve the following cell problems:

$$\begin{cases}\nabla_y\cdot[\nabla_y\boldsymbol{h}_v(\boldsymbol{x},\boldsymbol{y},t)K_v(\boldsymbol{x},\boldsymbol{y})^T]=-\nabla_y\cdot K_v(\boldsymbol{x},\boldsymbol{y})^T & \text{in } \Omega_v\times[0,T],\\ [\nabla_y\boldsymbol{h}_v(\boldsymbol{x},\boldsymbol{y},t)K_v(\boldsymbol{x},\boldsymbol{y})^T]\boldsymbol{n}=-K_v(\boldsymbol{x},\boldsymbol{y})^T\boldsymbol{n} & \text{on } \Gamma\times[0,T]\end{cases} \tag{3.29}$$

and

$$\begin{cases}\nabla_y\cdot[K_v(\boldsymbol{x},\boldsymbol{y})\nabla_y\tilde{h}_v(\boldsymbol{x},\boldsymbol{y},t)]=\nabla_y\cdot[K_v(\boldsymbol{x},\boldsymbol{y})\boldsymbol{b}_v^{(0)}(\boldsymbol{x},\boldsymbol{y},t)] & \text{in } \Omega_v\times[0,T],\\ [K_v(\boldsymbol{x},\boldsymbol{y})\nabla_y\tilde{h}_v(\boldsymbol{x},\boldsymbol{y},t)]\cdot\boldsymbol{n}=[K_v(\boldsymbol{x},\boldsymbol{y})\boldsymbol{b}_v^{(0)}(\boldsymbol{x},\boldsymbol{y},t)]\cdot\boldsymbol{n} & \text{on } \Gamma\times[0,T].\end{cases} \tag{3.30}$$

To ensure the solution uniqueness, we need to impose that $\langle\boldsymbol{h}_v(\boldsymbol{x},\boldsymbol{y},t)\rangle_{\Omega_v}=\boldsymbol{0}$ and $\langle\tilde{h}_v(\boldsymbol{x},\boldsymbol{y},t)\rangle_{\Omega_v}=0$, where the average operator $\langle(\bullet)\rangle_{\Omega_\gamma}$ is defined as

$$\langle(\bullet)\rangle_{\Omega_\gamma}=\frac{1}{|\Omega_\gamma|}\int_{\Omega_\gamma}(\bullet)\,\mathrm{d}\boldsymbol{y}. \tag{3.31}$$

Substituting the ansatz (3.28) into equation (3.19), we obtain the following Darcy's equation:

$$\begin{aligned}\boldsymbol{v}_v^{(0)}(\boldsymbol{x},\boldsymbol{y},t)&=-(K_v(\boldsymbol{x},\boldsymbol{y})+K_v(\boldsymbol{x},\boldsymbol{y})(\nabla_y\boldsymbol{h}_v(\boldsymbol{x},\boldsymbol{y},t))^T)\nabla_x p_v^{(0)}(\boldsymbol{x},t)\\&\quad-K_v(\boldsymbol{x},\boldsymbol{y})\nabla_y\tilde{h}_v(\boldsymbol{x},\boldsymbol{y},t)+K_v(\boldsymbol{x},\boldsymbol{y})\boldsymbol{b}_v^{(0)}(\boldsymbol{x},\boldsymbol{y},t).\end{aligned} \tag{3.32}$$

Putting together (3.21), (3.15), (3.16), (3.17) and (3.18) in Ω_m, we obtain the following *auxiliary Darcy–Brinkman problem in* $(v_m^{(0)}, p_m^{(1)})$:

$$\begin{cases} \eta \frac{\partial v_m^{(0)}}{\partial t}(\boldsymbol{x}, \boldsymbol{y}, t) = -\nabla_x p_m^{(0)}(\boldsymbol{x}, t) - \nabla_y p_m^{(1)}(\boldsymbol{x}, \boldsymbol{y}, t) \\ \qquad\qquad - K_m^{-1}(\boldsymbol{x}, \boldsymbol{y}) v_m^{(0)}(\boldsymbol{x}, \boldsymbol{y}, t) + \mu^* \Delta_y v_m^{(0)}(\boldsymbol{x}, \boldsymbol{y}, t) \\ \qquad\qquad + \boldsymbol{b}_m^{(0)}(\boldsymbol{x}, \boldsymbol{y}, t) & \text{in } \Omega_m \times [0, T], \\ \nabla_y \cdot v_m^{(0)}(\boldsymbol{x}, \boldsymbol{y}, t) = 0 & \text{in } \Omega_m \times [0, T], \\ v_m^{(0)}(\boldsymbol{x}, \boldsymbol{y}, t) \cdot \boldsymbol{n} = 0 & \text{on } \Gamma \times [0, T], \\ v_m^{(0)}(\boldsymbol{x}, \boldsymbol{y}, t) \cdot \boldsymbol{\tau} = -\frac{\sqrt{K_m(\boldsymbol{x}, \boldsymbol{y})}}{\alpha} [(\boldsymbol{n} \cdot \nabla_y) v_m^{(0)}(\boldsymbol{x}, \boldsymbol{y}, t)] \cdot \boldsymbol{\tau} & \text{on } \Gamma \times [0, T], \\ v_m^{(0)}(\boldsymbol{x}, \boldsymbol{y}, 0) = v_{m,0}^{(0)}(\boldsymbol{x}, \boldsymbol{y}) & \text{in } \Omega_m. \end{cases} \tag{3.33}$$

We apply the Fourier transform defined by

$$\mathcal{F}[\phi(t)] = \hat{\phi}(\omega) = \int_{-\infty}^{\infty} \phi(t) \mathrm{e}^{-2\pi i t \omega} \, \mathrm{d}t \tag{3.34}$$

to system (3.33), and we obtain (note that the initial condition can be written as $\delta(t) v_{m,0}^{(0)}(\boldsymbol{x}, \boldsymbol{y})$, where $\delta(t)$ is the *Dirac delta*)

$$\begin{aligned} 2\pi i \omega \eta \hat{v}_m^{(0)}(\boldsymbol{x}, \boldsymbol{y}, \omega) &= -\nabla_x \hat{p}_m^{(0)}(\boldsymbol{x}, \omega) - \nabla_y \hat{p}_m^{(1)}(\boldsymbol{x}, \boldsymbol{y}, \omega) - K_m^{-1}(\boldsymbol{x}, \boldsymbol{y}) \hat{v}_m^{(0)}(\boldsymbol{x}, \boldsymbol{y}, \omega) \\ &\quad + \mu^* \Delta_y \hat{v}_m^{(0)}(\boldsymbol{x}, \boldsymbol{y}, \omega) + \hat{\boldsymbol{b}}_m^{(0)}(\boldsymbol{x}, \boldsymbol{y}, \omega) + v_{m,0}^{(0)}(\boldsymbol{x}, \boldsymbol{y}) \quad \text{in } \Omega_m \times (-\infty, \infty), \end{aligned} \tag{3.35}$$

$$\nabla_y \cdot \hat{v}_m^{(0)}(\boldsymbol{x}, \boldsymbol{y}, \omega) = 0 \quad \text{in } \Omega_m \times (-\infty, \infty), \tag{3.36}$$

$$\hat{v}_m^{(0)}(\boldsymbol{x}, \boldsymbol{y}, \omega) \cdot \boldsymbol{n} = 0 \quad \text{on } \Gamma \times (-\infty, \infty) \tag{3.37}$$

and

$$\hat{v}_m^{(0)}(\boldsymbol{x}, \boldsymbol{y}, \omega) \cdot \boldsymbol{\tau} = -\frac{\sqrt{K_m(\boldsymbol{x}, \boldsymbol{y})}}{\alpha} [(\boldsymbol{n} \cdot \nabla_y) \hat{v}_m^{(0)}(\boldsymbol{x}, \boldsymbol{y}, \omega)] \cdot \boldsymbol{\tau} \quad \text{on } \Gamma \times (-\infty, \infty). \tag{3.38}$$

We have a linear problem and $\nabla_x \hat{p}_m^{(0)}$ depends on the macroscale only; hence we formulate an ansatz for the solution

$$\hat{p}_m^{(1)}(\boldsymbol{x}, \boldsymbol{y}, \omega) = -\hat{\boldsymbol{h}}_m(\boldsymbol{x}, \boldsymbol{y}, \omega) \cdot \nabla_x \hat{p}_m^{(0)}(\boldsymbol{x}, \omega) + \hat{\tilde{h}}_m(\boldsymbol{x}, \boldsymbol{y}, \omega) \tag{3.39}$$

and

$$\hat{v}_m^{(0)}(\boldsymbol{x}, \boldsymbol{y}, \omega) = -\hat{Q}_m(\boldsymbol{x}, \boldsymbol{y}, \omega) \nabla_x \hat{p}_m^{(0)}(\boldsymbol{x}, \omega) + \hat{\tilde{\boldsymbol{q}}}_m(\boldsymbol{x}, \boldsymbol{y}, \omega). \tag{3.40}$$

We have that (3.39) and (3.40) are the unique solutions of the auxiliary Darcy–Brinkman problem (3.33) provided that the auxiliary second rank tensor $\hat{Q}_\gamma$, the auxiliary vectors $\hat{\boldsymbol{h}}_\gamma$, $\hat{\tilde{\boldsymbol{q}}}_\gamma$ and the auxiliary scalar function $\hat{\tilde{h}}_\gamma$ solve the following cell problems:

$$\begin{cases} -2\pi i \omega \eta \hat{Q}_m(\boldsymbol{x}, \boldsymbol{y}, \omega) = -I + (\nabla_y \hat{\boldsymbol{h}}_m(\boldsymbol{x}, \boldsymbol{y}, \omega))^T + K_m^{-1}(\boldsymbol{x}, \boldsymbol{y}) \hat{Q}_m(\boldsymbol{x}, \boldsymbol{y}, \omega) \\ \qquad\qquad - \mu^* \Delta_y \hat{Q}_m(\boldsymbol{x}, \boldsymbol{y}, \omega) & \text{in } \Omega_m \times (-\infty, \infty), \\ \nabla_y \cdot \hat{Q}_m(\boldsymbol{x}, \boldsymbol{y}, \omega) = \boldsymbol{0} & \text{in } \Omega_m \times (-\infty, \infty), \\ \hat{Q}_m^T(\boldsymbol{x}, \boldsymbol{y}, \omega) \boldsymbol{n} = \boldsymbol{0} & \text{on } \Gamma \times (-\infty, \infty), \\ \hat{Q}_m^T(\boldsymbol{x}, \boldsymbol{y}, \omega) \boldsymbol{\tau} = -\frac{\sqrt{K_m}}{\alpha} [(\nabla_y \hat{Q}_m^T(\boldsymbol{x}, \boldsymbol{y}, \omega)) \boldsymbol{n}] \boldsymbol{\tau} & \text{on } \Gamma \times (-\infty, \infty), \end{cases} \tag{3.41}$$

and

$$\begin{cases} 2\pi i \omega \eta \hat{\tilde{\boldsymbol{q}}}_m(\boldsymbol{x}, \boldsymbol{y}, \omega) = -K_m^{-1}(\boldsymbol{x}, \boldsymbol{y}) \hat{\tilde{\boldsymbol{q}}}_m(\boldsymbol{x}, \boldsymbol{y}, \omega) + \mu^* \Delta_y \hat{\tilde{\boldsymbol{q}}}_m(\boldsymbol{x}, \boldsymbol{y}) \\ \qquad\qquad - \nabla_y \hat{\tilde{h}}_m(\boldsymbol{x}, \boldsymbol{y}, \omega) + \hat{\boldsymbol{b}}_m^{(0)}(\boldsymbol{x}, \boldsymbol{y}, \omega) + v_{m,0}^{(0)}(\boldsymbol{x}, \boldsymbol{y}) & \text{in } \Omega_m \times (-\infty, \infty), \\ \nabla_y \cdot \hat{\tilde{\boldsymbol{q}}}_m(\boldsymbol{x}, \boldsymbol{y}, \omega) = 0 & \text{in } \Omega_m \times (-\infty, \infty), \\ \hat{\tilde{\boldsymbol{q}}}_m(\boldsymbol{x}, \boldsymbol{y}, \omega) \cdot \boldsymbol{n} = 0 & \text{on } \Gamma \times (-\infty, \infty), \\ \hat{\tilde{\boldsymbol{q}}}_m(\boldsymbol{x}, \boldsymbol{y}, \omega) \cdot \boldsymbol{\tau} = -\frac{\sqrt{K_m(\boldsymbol{x}, \boldsymbol{y})}}{\alpha} [(\boldsymbol{n} \cdot \nabla_y) \hat{\tilde{\boldsymbol{q}}}_m(\boldsymbol{x}, \boldsymbol{y}, \omega)] \cdot \boldsymbol{\tau} & \text{on } \Gamma \times (-\infty, \infty). \end{cases} \tag{3.42}$$

If we apply the inverse Fourier transform $\mathcal{F}^{-1}$ to (3.41) and (3.42), we obtain

$$\begin{cases} \eta \frac{\partial Q_m}{\partial t}(\boldsymbol{x}, \boldsymbol{y}, t) = -K_m^{-1}(\boldsymbol{x}, \boldsymbol{y}) Q_m(\boldsymbol{x}, \boldsymbol{y}, t) + \mu^* \Delta_y Q_m^T(\boldsymbol{x}, \boldsymbol{y}, t) \\ \qquad\qquad + \delta(t) I - (\nabla_y \boldsymbol{h}_m(\boldsymbol{x}, \boldsymbol{y}, t))^T & \text{in } \Omega_m \times [0, T], \\ \nabla_y \cdot Q_m(\boldsymbol{x}, \boldsymbol{y}, t) = \boldsymbol{0} & \text{in } \Omega_m \times [0, T], \\ Q_m^T(\boldsymbol{x}, \boldsymbol{y}, t)\boldsymbol{n} = \boldsymbol{0} & \text{on } \Gamma \times [0, T], \\ Q_m^T(\boldsymbol{x}, \boldsymbol{y}, t)\boldsymbol{\tau} = -\frac{\sqrt{K_m}}{\alpha} [\nabla_y Q_m^T(\boldsymbol{x}, \boldsymbol{y}, t)\boldsymbol{n}]\boldsymbol{\tau} & \text{on } \Gamma \times [0, T], \\ Q_m(\boldsymbol{x}, \boldsymbol{y}, 0) = 0 & \text{in } \Omega_m, \end{cases} \tag{3.43}$$

and

$$\begin{cases} \eta \frac{\partial \tilde{\boldsymbol{q}}_m}{\partial t}(\boldsymbol{x}, \boldsymbol{y}, t) = -K_m^{-1}(\boldsymbol{x}, \boldsymbol{y}) \tilde{\boldsymbol{q}}_m(\boldsymbol{x}, \boldsymbol{y}, t) + \mu^* \Delta_y \tilde{\boldsymbol{q}}_m(\boldsymbol{x}, \boldsymbol{y}, t) \\ \qquad\qquad - \nabla_y \tilde{h}_m(\boldsymbol{x}, \boldsymbol{y}, t) + \boldsymbol{b}_m^{(0)}(\boldsymbol{x}, \boldsymbol{y}, t) & \text{in } \Omega_m \times [0, T], \\ \nabla_y \cdot \tilde{\boldsymbol{q}}_m(\boldsymbol{x}, \boldsymbol{y}, t) = 0 & \text{in } \Omega_m \times [0, T], \\ \tilde{\boldsymbol{q}}_m(\boldsymbol{x}, \boldsymbol{y}, t) \cdot \boldsymbol{n} = 0 & \text{on } \Gamma \times [0, T], \\ \tilde{\boldsymbol{q}}_m(\boldsymbol{x}, \boldsymbol{y}, t) \cdot \boldsymbol{\tau} = -\frac{\sqrt{K_m}}{\alpha} [(\boldsymbol{n} \cdot \nabla_y) \tilde{\boldsymbol{q}}_m(\boldsymbol{x}, \boldsymbol{y}, t)] \cdot \boldsymbol{\tau} & \text{on } \Gamma \times [0, T], \\ \tilde{\boldsymbol{q}}_m(\boldsymbol{x}, \boldsymbol{y}, 0) = \boldsymbol{v}_{m,0}^{(0)}(\boldsymbol{x}, \boldsymbol{y}) & \text{in } \Omega_m. \end{cases} \tag{3.44}$$

We note that system (3.44) gives a null result if the initial condition $\boldsymbol{v}_{m,0}^{(0)}(\boldsymbol{x}, \boldsymbol{y})$ and the multiscale force $\boldsymbol{b}_m$ are both zero.

For system (3.43), we define the quantities

$$\bar{\boldsymbol{h}}_m(\boldsymbol{x}, \boldsymbol{y}, t) = \int_{-\epsilon_2}^{t} \boldsymbol{h}_m(\boldsymbol{x}, \boldsymbol{y}, s)\, \mathrm{d}s \quad \text{and} \quad \bar{Q}_m(\boldsymbol{x}, \boldsymbol{y}, t) = \int_{-\epsilon_2}^{t} Q_m(\boldsymbol{x}, \boldsymbol{y}, s)\, \mathrm{d}s, \tag{3.45}$$

where ϵ_2 is a small number >0, so that

$$\boldsymbol{h}_m(\boldsymbol{x}, \boldsymbol{y}, t) = \frac{\partial \bar{\boldsymbol{h}}_m}{\partial t}(\boldsymbol{x}, \boldsymbol{y}, t), \quad Q_m(\boldsymbol{x}, \boldsymbol{y}, t) = \frac{\partial \bar{Q}_m}{\partial t}(\boldsymbol{x}, \boldsymbol{y}, t); \tag{3.46}$$

substituting these equations into (3.43) and integrating over time, we have

$$\begin{cases} \eta \frac{\partial \bar{Q}_m}{\partial t}(\boldsymbol{x}, \boldsymbol{y}, t) = -K_m^{-1}(\boldsymbol{x}, \boldsymbol{y}) \bar{Q}_m(\boldsymbol{x}, \boldsymbol{y}, t) \\ \qquad\qquad + \mu^* \Delta_y \bar{Q}_m(\boldsymbol{x}, \boldsymbol{y}, t) + I - (\nabla_y \bar{\boldsymbol{h}}_m(\boldsymbol{x}, \boldsymbol{y}, t))^T & \text{in } \Omega_m \times [0, T], \\ \nabla_y \cdot \bar{Q}_m(\boldsymbol{x}, \boldsymbol{y}, t) = \boldsymbol{0} & \text{in } \Omega_m \times [0, T], \\ \bar{Q}_m^T(\boldsymbol{x}, \boldsymbol{y}, t)\boldsymbol{n} = \boldsymbol{0} & \text{on } \Gamma \times [0, T], \\ \bar{Q}_m^T(\boldsymbol{x}, \boldsymbol{y}, t)\boldsymbol{\tau} = -\frac{\sqrt{K_m}}{\alpha} [(\nabla_y \bar{Q}_m^T(\boldsymbol{x}, \boldsymbol{y}, t))\boldsymbol{n}]\boldsymbol{\tau} & \text{on } \Gamma \times [0, T], \\ \bar{Q}_m(\boldsymbol{x}, \boldsymbol{y}, 0) = 0 & \text{in } \Omega_m. \end{cases} \tag{3.47}$$

Applying the inverse Fourier transform $\mathcal{F}^{-1}$ to the ansatz (3.39)–(3.40), we obtain

$$\begin{aligned} \boldsymbol{v}_m^{(0)}(\boldsymbol{x}, \boldsymbol{y}, t) &= -\mathcal{F}^{-1}[\hat{Q}_m(\boldsymbol{x}, \boldsymbol{y}, \omega) \nabla_x \hat{p}_m^{(0)}(\boldsymbol{x}, \omega)] + \tilde{\boldsymbol{q}}_m(\boldsymbol{x}, \boldsymbol{y}, t) \\ &= -\int_0^t \frac{\partial \bar{Q}_m}{\partial t}(\boldsymbol{x}, \boldsymbol{y}, t - s) \nabla_x p_m^{(0)}(\boldsymbol{x}, s)\, \mathrm{d}s + \tilde{\boldsymbol{q}}_m(\boldsymbol{x}, \boldsymbol{y}, t), \end{aligned} \tag{3.48}$$

which is in the form of a *Darcy equation with memory effects* [8,26,27].

By the same computations, we obtain

$$p_m^{(1)}(\boldsymbol{x}, \boldsymbol{y}, t) = -\int_0^t \frac{\partial \bar{\boldsymbol{h}}_m^T}{\partial t}(\boldsymbol{x}, \boldsymbol{y}, t - s) \nabla_x p_m^{(0)}(\boldsymbol{x}, s)\, \mathrm{d}s + \tilde{h}_m(\boldsymbol{x}, \boldsymbol{y}, t). \tag{3.49}$$

Moreover, we need that $\langle \bar{\boldsymbol{h}}_m(\boldsymbol{x}, \boldsymbol{y}, t) \rangle_{\Omega_m} = \boldsymbol{0}$ and $\langle \tilde{h}_m(\boldsymbol{x}, \boldsymbol{y}, t) \rangle_{\Omega_m} = 0$ to ensure the uniqueness of the solution, where $\langle \cdot \rangle_{\Omega_m}$ is the average operator defined in (3.31).

4. Derivation of the macroscopic model

We now apply the average operator (3.31)–(3.48)

$$\langle \boldsymbol{v}_m^{(0)}(\boldsymbol{x}, \boldsymbol{y}, t) \rangle_{\Omega_m} = -\int_0^t \left\langle \frac{\partial \bar{Q}_m}{\partial t}(\boldsymbol{x}, \boldsymbol{y}, t - s) \right\rangle_{\Omega_m} \nabla_x p_m^{(0)}(\boldsymbol{x}, s)\, \mathrm{d}s + \langle \tilde{\boldsymbol{q}}_m(\boldsymbol{x}, \boldsymbol{y}, t) \rangle_{\Omega_m},$$

where $\bar{Q}_m$ and $\tilde{\boldsymbol{q}}_m$ are computed by problems (3.47) and (3.44), respectively.

Applying the average operator (3.31) to equation (3.22), we obtain (using the macroscopic uniformity)

$$\nabla_x \cdot \langle \boldsymbol{v}_m^{(0)}(\boldsymbol{x}, \boldsymbol{y}, t)\rangle_{\Omega_m} + \langle \nabla_y \cdot \boldsymbol{v}_m^{(1)}(\boldsymbol{x}, \boldsymbol{y}, t)\rangle_{\Omega_m} = 0, \tag{4.1}$$

where, by the divergence theorem and the interface conditions (3.23), we have, for the phase Ω_m

$$\langle \nabla_y \cdot \boldsymbol{v}_m^{(1)}(\boldsymbol{x}, \boldsymbol{y}, t)\rangle_{\Omega_m} = \frac{1}{|\Omega_m|}\int_{\Omega_m} \nabla_y \cdot \boldsymbol{v}_m^{(1)}(\boldsymbol{x}, \boldsymbol{y}, t)\,\mathrm{d}\boldsymbol{y} = \frac{\bar{L}_p S}{|\Omega_m|}[p_m^{(0)}(\boldsymbol{x}, t) - p_v^{(0)}(\boldsymbol{x}, t) - \bar{p}(t)], \tag{4.2}$$

and hence

$$\nabla_x \cdot \langle \boldsymbol{v}_m^{(0)}(\boldsymbol{x}, \boldsymbol{y}, t)\rangle_{\Omega_m} = -\frac{\bar{L}_p S}{|\Omega_m|}[p_m^{(0)}(\boldsymbol{x}, t) - p_v^{(0)}(\boldsymbol{x}, t) - \bar{p}(t)]. \tag{4.3}$$

For the Darcy problem on the phase Ω_v, applying the average operator (3.31) to equation (3.32), we obtain

$$\begin{aligned}\langle \boldsymbol{v}_v^{(0)}(\boldsymbol{x}, \boldsymbol{y}, t)\rangle_{\Omega_v} = &-\langle K_v(\boldsymbol{x}, \boldsymbol{y}) + K_v(\boldsymbol{x}, \boldsymbol{y})(\nabla_y \boldsymbol{h}_v(\boldsymbol{x}, \boldsymbol{y}, t))^T\rangle_{\Omega_v} \nabla_x p_v^{(0)}(\boldsymbol{x}, t)\\ &- \langle K_v(\boldsymbol{x}, \boldsymbol{y})\nabla_y \tilde{h}_v(\boldsymbol{x}, \boldsymbol{y}, t)\rangle_{\Omega_v} + \langle K_v(\boldsymbol{x}, \boldsymbol{y})\boldsymbol{b}_v^{(0)}(\boldsymbol{x}, \boldsymbol{y}, t)\rangle_{\Omega_v}.\end{aligned} \tag{4.4}$$

We apply the average operator and the divergence theorem to equation (3.20) and, following the same computations as before, we obtain

$$\nabla_x \cdot \langle \boldsymbol{v}_v^{(0)}(\boldsymbol{x}, \boldsymbol{y}, t)\rangle_{\Omega_v} + \langle \nabla_y \cdot \boldsymbol{v}_v^{(1)}(\boldsymbol{x}, \boldsymbol{y}, t)\rangle_{\Omega_v} = 0, \tag{4.5}$$

and using the divergence theorem and the interface conditions (3.23)

$$\langle \nabla_y \cdot \boldsymbol{v}_v^{(1)}(\boldsymbol{x}, \boldsymbol{y}, t)\rangle_{\Omega_v} = \frac{1}{|\Omega_v|}\int_{\Omega_v} \nabla_y \cdot \boldsymbol{v}_v^{(1)}(\boldsymbol{x}, \boldsymbol{y}, t)\,\mathrm{d}\boldsymbol{y} = -\frac{\bar{L}_p S}{|\Omega_v|}[p_m^{(0)}(\boldsymbol{x}, t) - p_v^{(0)}(\boldsymbol{x}, t) - \bar{p}(t)], \tag{4.6}$$

where we used the fact that $\boldsymbol{n}_v = -\boldsymbol{n}$; hence

$$\nabla_x \cdot \langle \boldsymbol{v}_v^{(0)}(\boldsymbol{x}, \boldsymbol{y}, t)\rangle_{\Omega_v} = \frac{\bar{L}_p S}{|\Omega_v|}[p_m^{(0)}(\boldsymbol{x}, t) - p_v^{(0)}(\boldsymbol{x}, t) - \bar{p}(t)]. \tag{4.7}$$

The total coarse velocity $\boldsymbol{u}_C$ is

$$\begin{aligned}\boldsymbol{u}_C =&|\Omega_m|\langle \boldsymbol{v}_m^{(0)}(\boldsymbol{x}, \boldsymbol{y}, t)\rangle_{\Omega_m} + |\Omega_v|\langle \boldsymbol{v}_v^{(0)}(\boldsymbol{x}, \boldsymbol{y}, t)\rangle_{\Omega_v}\\ =&-|\Omega_m|\int_0^t \langle \frac{\partial \bar{Q}_m}{\partial t}(\boldsymbol{x}, \boldsymbol{y}, t-s)\rangle_{\Omega_m} \nabla_x p_m^{(0)}(\boldsymbol{x}, s)\,\mathrm{d}s + |\Omega_m|\langle \tilde{\boldsymbol{q}}_m(\boldsymbol{x}, \boldsymbol{y}, t)\rangle_{\Omega_m}\\ &- |\Omega_v|\langle K_v(\boldsymbol{x}, \boldsymbol{y}) + K_v(\boldsymbol{x}, \boldsymbol{y})(\nabla_y \boldsymbol{h}_v(\boldsymbol{x}, \boldsymbol{y}))^T\rangle_{\Omega_v} \nabla_x p_v^{(0)}(\boldsymbol{x})\\ &- |\Omega_v|\langle K_v(\boldsymbol{x}, \boldsymbol{y})\nabla_y \tilde{h}_v(\boldsymbol{x}, \boldsymbol{y})\rangle_{\Omega_v} + |\Omega_v|\langle K_v(\boldsymbol{x}, \boldsymbol{y})\boldsymbol{b}_v^{(0)}(\boldsymbol{x}, \boldsymbol{y})\rangle_{\Omega_v}.\end{aligned} \tag{4.8}$$

Substituting (4.1) into equation (4.3) and (4.4) into equation (4.7), we obtain

$$\begin{aligned}\nabla_x \cdot \left(\int_0^t \left\langle \frac{\partial \bar{Q}}{\partial t}(\boldsymbol{x}, \boldsymbol{y}, t-s)\right\rangle_{\Omega_m} \nabla_x p_m^{(0)}(\boldsymbol{x}, s)\,\mathrm{d}s\right) = &\nabla_x \cdot \langle \tilde{\boldsymbol{q}}_m(\boldsymbol{x}, \boldsymbol{y}, t)\rangle_{\Omega_m}\\ &+ \frac{\bar{L}_p S}{|\Omega_m|}[p_m^{(0)}(\boldsymbol{x}, t) - p_v^{(0)}(\boldsymbol{x}, t) - \bar{p}(t)]\end{aligned} \tag{4.9}$$

and

$$\begin{aligned}&\nabla_x \cdot \left(\langle K_v(\boldsymbol{x}, \boldsymbol{y}) + K_v(\boldsymbol{x}, \boldsymbol{y})(\nabla_y \boldsymbol{h}_v(\boldsymbol{x}, \boldsymbol{y}, t))^T\rangle_{\Omega_v} \nabla_x p_v^{(0)}(\boldsymbol{x}, t)\right)\\ &= \quad -\nabla_x \cdot \langle K_v(\boldsymbol{x}, \boldsymbol{y})\nabla_y \tilde{h}_v(\boldsymbol{x}, \boldsymbol{y}, t)\rangle_{\Omega_v}\\ &\quad + \nabla_x \cdot \langle K_v(\boldsymbol{x}, \boldsymbol{y})\boldsymbol{b}_v^{(0)}(\boldsymbol{x}, \boldsymbol{y}, t)\rangle_{\Omega_v} - \frac{\bar{L}_p S}{|\Omega_m|}[p_m^{(0)}(\boldsymbol{x}, t) - p_v^{(0)}(\boldsymbol{x}, t) - \bar{p}(t)].\end{aligned} \tag{4.10}$$

Equation (4.11) is the well-known diffusion problem related to the Darcy equation, where we can find additional terms that are related to the fluid exchange between phases and the multiscale forces [1,24]. When the multiscale force $\boldsymbol{b}_v$ is zero, the unique solution $\tilde{h}_v(\boldsymbol{x}, \boldsymbol{y}, t)$ of the system (3.30) is zero, and in this case, equation (4.11) becomes the Darcy equation with fluid exchange between phases as derived and solved in [2,3,68]. On the other hand, equation (4.10) is the Darcy equation diffusion problem with memory effect, with additional terms related to the multiscale forces [24], the fluid exchange between phases and the multiscale initial condition. We note that if the multiscale force $\boldsymbol{b}_m$ and the initial condition $\boldsymbol{v}_{m,0}$ are both zeros, the unique solution $\tilde{\boldsymbol{q}}_m$ of the system (3.44) is zero. Taking into account the time dependence of the problem, we obtain a very different model from the previous one [1–3,24,68]. However, even when ignoring the contributions related to the external volume loads and

the initial condition, the final model that we have obtained differs from the one in [8,26] due to the coupling and the fluid exchange between the Darcy equation with memory effect and the classical Darcy equation and due to the Darcy–Brinkman type cell problem which needs to be solved to compute the hydraulic conductivity $\langle \partial \bar{Q}/\partial t \rangle_{\Omega_m}$ for the matrix compartment Ω_m.

Now we dimensionalize equations (4.1), (4.3), (4.4) and (4.7). We write the equations in dimensional form because, with regard to their application to the lymph node, this makes it easier to interpret the results and compare them with other studies on the same topic. We have

$$|\Omega_m| = \frac{|\Omega_m^{\text{tot}}|}{|\Omega|}, \quad |\Omega_v| = \frac{|\Omega_v^{\text{tot}}|}{|\Omega|} \quad \text{and} \quad S = \frac{S^{\text{tot}} d}{|\Omega|}, \tag{4.11}$$

where $|\Omega|$ is the lymph node total volume, $|\Omega_m^{\text{tot}}|$ is the phase m total volume, $|\Omega_v^{\text{tot}}|$ is the phase v total volume and S^{tot} is the total vessel surface. Hence equations (4.1), (4.4), (4.5) and (4.8) are (in dimensional form)

$$\begin{aligned} \langle \boldsymbol{v}_m^{(0)}(\boldsymbol{x}, \boldsymbol{y}, t) \rangle_{\Omega_m} &= -\frac{d^2}{\mu} \int_0^t \left\langle \frac{\partial \bar{Q}}{\partial t}(\boldsymbol{x}, \boldsymbol{y}, t-s) \right\rangle_{\Omega_m} \nabla_x p_m^{(0)}(\boldsymbol{x}, s)\, \mathrm{d}s \\ &\quad + U \langle \tilde{\boldsymbol{q}}_{m,1}(\boldsymbol{x}, \boldsymbol{y}, t) \rangle_{\Omega_m} + U \langle \tilde{\boldsymbol{q}}_{m,2}(\boldsymbol{x}, \boldsymbol{y}, t) \rangle_{\Omega_m}, \end{aligned} \tag{4.12}$$

$$\nabla_x \cdot \langle \boldsymbol{v}_m^{(0)}(\boldsymbol{x}, \boldsymbol{y}, t) \rangle_{\Omega_m} = -\frac{L_p S^{\text{tot}}}{|\Omega_m^{\text{tot}}|} [p_m^{(0)}(\boldsymbol{x}, t) - p_v^{(0)}(\boldsymbol{x}, t) - \bar{p}(t)], \tag{4.13}$$

$$\begin{aligned} \langle \boldsymbol{v}_v^{(0)}(\boldsymbol{x}, \boldsymbol{y}, t) \rangle_{\Omega_v} &= -\frac{d^2}{\mu} \langle K_v(\boldsymbol{x}, \boldsymbol{y}) + K_v(\boldsymbol{x}, \boldsymbol{y})(\nabla_y \boldsymbol{h}_v(\boldsymbol{x}, \boldsymbol{y}, t))^T \rangle_{\Omega_v} \nabla_x p_v^{(0)}(\boldsymbol{x}, t) \\ &\quad - U \langle K_v(\boldsymbol{x}, \boldsymbol{y}) \nabla_y \tilde{h}_v(\boldsymbol{x}, \boldsymbol{y}, t) \rangle_{\Omega_v} + U \langle K_v(\boldsymbol{x}, \boldsymbol{y}) \boldsymbol{b}_v^{(0)}(\boldsymbol{x}, \boldsymbol{y}, t) \rangle_{\Omega_v} \end{aligned} \tag{4.14}$$

and

$$\nabla_x \cdot \langle \boldsymbol{v}_v^{(0)}(\boldsymbol{x}, \boldsymbol{y}, t) \rangle_{\Omega_v} = \frac{L_p S^{\text{tot}}}{|\Omega_v^{\text{tot}}|} [p_m^{(0)}(\boldsymbol{x}, t) - p_v^{(0)}(\boldsymbol{x}, t) - \bar{p}(t)]. \tag{4.15}$$

5. Explicit solution

In this section, we explicitly solve the problems given in §4.

For simplicity, we suppose $\boldsymbol{v}_{m,0} = \boldsymbol{0}$, $\boldsymbol{b}_m = \boldsymbol{0}$, $\boldsymbol{b}_v = \boldsymbol{0}$; hence the unique solution of problems (3.30) and (3.44) is zero. Moreover, we assume the isotropy of both the porous media, which means

$$\bar{K}_v = \bar{K}_v I, \quad \bar{K}_m = \bar{K}_m(t) I, \tag{5.1}$$

where $\bar{K}_v$ and $\bar{K}_m(t)$ correspond to $d^2/\mu \langle K_v + K_v(\nabla_y \boldsymbol{h}_v)^T \rangle_{\Omega_v}$ and $d^2/\mu \langle Q_m(\boldsymbol{y}, t) \rangle_{\Omega_m}$, respectively. We have that $\bar{K}_v$ is constant in space due to the geometry and the hypotheses used, and it is found solving the cell problem (3.29) using COMSOL Multiphysics (see §6 for more details about the numerical simulations of the cell problem). We have that the dimensional value for the vessel hydraulic conductivity $K_v d^2/\mu$ is computed using the Kozeny–Carman formula, i.e. $(1/c_0)(|\Omega_v^{\text{tot}}|/S^{\text{tot}})^2$; see table 1 and [1, appendix B] for more details. For phase m, due to the memory term that appears in equation (4.1), it is better to work in the frequency domain to find an explicit solution. Hence, applying the average operator (3.31) to the ansatz (3.40), we have in dimensional form

$$\langle \hat{\boldsymbol{v}}_m^{(0)}(\boldsymbol{x}, \boldsymbol{y}, \omega) \rangle_{\Omega_m} = -\hat{\bar{K}}_m(\omega) \nabla_x \hat{p}_m^{(0)}(\boldsymbol{x}, \omega) = -\frac{d^2}{\mu} \langle \hat{Q}_m(\boldsymbol{y}, \omega) \rangle_{\Omega_m} \nabla_x \hat{p}_m^{(0)}(\boldsymbol{x}, \omega). \tag{5.2}$$

We find $\hat{Q}_m(\boldsymbol{y}, \omega)$ by solving the cell problem (3.41) using COMSOL Multiphysics, with $\alpha = 1$ (see §6 for more information about the numerical simulations of the cell problem and figure 2 for the results).

As we are working in the frequency domain, we apply the Fourier transform (3.34) to (4.9)–(4.9). We consider a spherical domain Ω with radius R, denoting by r the radial coordinate, θ the polar coordinate and ϕ the azimuthal angle. Moreover, we assume axisymmetry with respect to the azimuthal angle ϕ. Hence, we obtain the following problem:

$$\begin{cases} \Delta \hat{p}_v^{(0)}(r, \theta, \omega) = -M_v[\hat{p}_m^{(0)}(r, \theta, \omega) - \hat{p}_v^{(0)}(r, \theta, \omega) - \bar{p}(\omega)] & r < R, \ \theta \in [0, 2\pi[, \ \omega \in (-\infty, \infty), \\ \Delta \hat{p}_m^{(0)}(r, \theta, \omega) = M_m(\omega)[\hat{p}_m^{(0)}(r, \theta, \omega) - \hat{p}_v^{(0)}(r, \theta, \omega) - \bar{p}(\omega)] & r < R, \ \theta \in [0, 2\pi[, \ \omega \in (-\infty, \infty), \\ \hat{p}_v^{(0)}(R, \theta, \omega) = \hat{\bar{p}}_v(\theta, \omega), \quad \hat{p}_m^{(0)}(R, \theta, \omega) = \hat{\bar{p}}_m(\theta, \omega) & \theta \in [0, 2\pi[, \ \omega \in (-\infty, \infty), \\ \text{non-degeneracy} & r = 0, \ \theta \in [0, 2\pi[, \ \omega \in (-\infty, \infty), \end{cases} \tag{5.3}$$

where R is the sphere radius, $M_v = L_p S^{\text{tot}}/|\Omega_v^{\text{tot}}|\bar{K}_v$, $M_m(\omega) = L_p S^{\text{tot}}/|\Omega_m^{\text{tot}}|\hat{\bar{K}}_m(\omega)$, and $\hat{\bar{p}}_v$ and $\hat{\bar{p}}_m$ are the Fourier transforms of the given boundary condition.

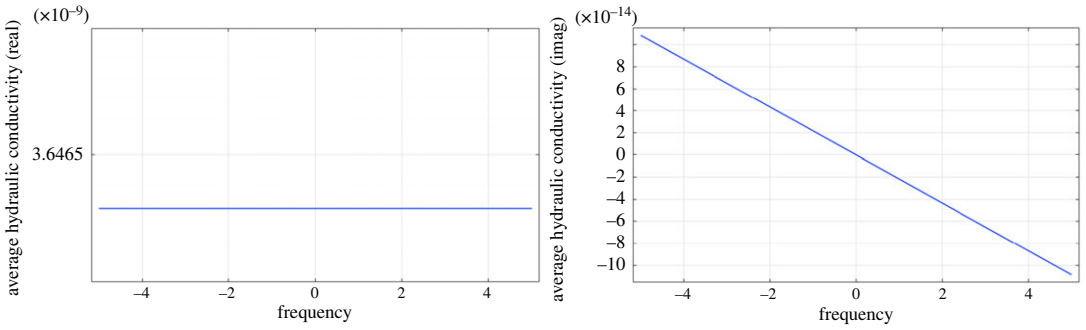

Figure 2. The Fourier transform of the dimensional average hydraulic conductivity in $mm^3\,s\,mg^{-1}$ calculated numerically with physiological values of the lymph node (table 1).

Table 1. Physiological and estimated parameters; see [1, appendix] for more details.

name	physiological range/value	description
R	0.49 mm	LC radius [39,59]
μ	1 mg mm^{-1} s^{-1}	viscosity [36,37]
ϕ	0.75	porosity [55]
μ_e	$\frac{\mu}{\phi}$	effective viscosity [10,70–72]
ρ_0	1 mg mm^{-3}	density [36,37]
$\hat{\mathrm{K}}_m$	3.84×10^{-9} mm^2	interstitial permeability [46,55]
σ	0.88–0.9	Staverman's coefficient [47,53,54,57]
$\pi_v - \pi_m$	3.41×10^5–2.08×10^6 mPa	osmotic pressure difference [47,53,54,57,73–76]
L_p	5.475×10^{-12}–3.67×10^{-8} mm s^{-1} mPa^{-1}	hydraulic conductivity of the blood vessel walls [47,53,54,57]
$\bar{p}_v$	6.67×10^5–1.066×10^6 mPa	mean blood vessel pressure [47,53,54,57]
S^{tot}	13.4 mm^2	surface of the blood vessels [48,49]
$\lvert\Omega_v^{\mathrm{tot}}\rvert$	0.0322 mm^3	volume of the blood vessel [48]
N	1310	cell number [1, appendix B]
r_c	1.7×10^{-3} mm	cylinders radius (microscale) [1, appendix B]
d	2×10^{-2} mm	cylinder mean distance (microscale) [1, appendix B]
L	1 mm	characteristic length (macroscale)
$K_v\,(d^2/\mu)$	1.1×10^{-6} $mm^3\,s\,mg^{-1}$	blood vessels hydraulic conductivity, calculated using the Kozeny–Carman formula [1,77,78]
$\boldsymbol{b}_m$, $\boldsymbol{b}_v$	**0**	body forces
$\bar{\hat{K}}_m$	figure 2	macroscopic interstitial hydraulic conductivity (solving system (3.41))
$\bar{K}_v$	4.12×10^{-7} $mm^3\,s\,mg^{-1}$	macroscopic blood hydraulic conductivity (solving system (3.29))

Following the computations presented in [1, appendix A], we obtain the following solutions (see [1, appendix A]):

$$\hat{p}_m^{(0)}(r,\zeta,\omega) = \sum_{n=0}^{\infty}\left[c_1^{(n)}(\omega)r^n + \frac{M_m(\omega)\tilde{A}_n(\omega)}{M(\omega)}\frac{1}{\sqrt{r}}I_{n+(1/2)}\left(\sqrt{M(\omega)}r\right)\right]P_n(\zeta) \tag{5.4}$$

and

$$\hat{p}_v^{(0)}(r,\zeta,\omega)=\sum_{n=0}^{\infty}\left[d_1^{(n)}(\omega)r^n-\frac{M_v\tilde{A}_n(\omega)}{M(\omega)}\frac{1}{\sqrt{r}}I_{n+(1/2)}\left(\sqrt{M(\omega)}r\right)\right]P_n(\zeta), \tag{5.5}$$

where $\zeta=\cos\theta$, $M(\omega)=M_v+M_m(\omega)$, I_n is the modified Bessel function of the first kind of order n, P_n is the Legendre polynomial of the first kind of order n, and (the following relations are obtained from [1, appendix A])

$$\tilde{A}_0(\omega)=\frac{[b^{(0)}(\omega)-\bar{p}(\omega)]\sqrt{R}}{I_{(1/2)}\left(\sqrt{M(\omega)}R\right)}\quad\text{for } n=0,\quad \tilde{A}_n(\omega)=\frac{b^{(n)}(\omega)\sqrt{R}}{I_{n+(1/2)}\left(\sqrt{M(\omega)}R\right)}\quad\text{for } n\geq 1, \tag{5.6}$$

$$c_1^{(n)}(\omega)=\frac{\left[b_m^{(n)}(\omega)-(M_m(\omega)\tilde{A}_n(\omega)/M(\omega)\sqrt{R})I_{n+(1/2)}\left(\sqrt{M(\omega)}R\right)\right]}{R^n}, \tag{5.7}$$

$$d_1^{(n)}(\omega)=\frac{\left[b_v^{(n)}(\omega)+(M_v\tilde{A}_n(\omega)/M(\omega)\sqrt{R})I_{n+(1/2)}\left(\sqrt{M(\omega)}R\right)\right]}{R^n}, \tag{5.8}$$

$$b^{(n)}(\omega)=\frac{1}{2}(2n+1)\int_{-1}^{1}[\hat{\bar{p}}_m(\zeta,\omega)-\hat{\bar{p}}_v(\zeta,\omega)]P_n(\zeta)d\zeta \tag{5.9}$$

and
$$b_m^{(n)}(\omega)=\frac{1}{2}(2n+1)\int_{-1}^{1}\hat{\bar{p}}_m(\zeta,\omega)P_n(\zeta)\,\mathrm{d}\zeta,\quad b_v^{(n)}(\omega)=\frac{1}{2}(2n+1)\int_{-1}^{1}\hat{\bar{p}}_v(\zeta,\omega)P_n(\zeta)\,\mathrm{d}\zeta. \tag{5.10}$$

Hence, we have, applying the inverse Fourier transform $\mathcal{F}^{-1}$ to (5.4) and (5.5)

$$p_m^{(0)}(r,\zeta,t)=\sum_{n=0}^{\infty}\mathcal{F}^{-1}\left[c_1^{(n)}(\omega)r^n+\frac{M_m(\omega)\tilde{A}_n(\omega)}{M(\omega)}\frac{1}{\sqrt{r}}I_{n+(1/2)}\left(\sqrt{M(\omega)}r\right)\right]P_n(\zeta) \tag{5.11}$$

and

$$p_v^{(0)}(r,\zeta,t)=\sum_{n=0}^{\infty}\mathcal{F}^{-1}\left[d_1^{(n)}(\omega)r^n-\frac{M_v\tilde{A}_n(\omega)}{M(\omega)}\frac{1}{\sqrt{r}}I_{n+(1/2)}\left(\sqrt{M(\omega)}r\right)\right]P_n(\zeta). \tag{5.12}$$

6. Cell problem numerical simulations

In this section, we discuss the numerical simulations used to find the solutions of the cell problems (3.29), (3.30), (3.41) and (3.42). We can see the geometry of the cell problems using the lymph node physiological data found in [1, appendix B] and summarized in table 1 in figure 1.

As we mentioned in §5, we suppose $\boldsymbol{u}_{m,0}=\mathbf{0}$, $\boldsymbol{f}_m=\mathbf{0}$, $\boldsymbol{f}_v=\mathbf{0}$, which means that the solutions of the problems (3.30) and (3.42) are zeros. Moreover, we suppose that both porous media are isotropic, which means

$$\bar{K}_v=\bar{K}_vI=\frac{d^2}{\mu}\langle K_v+K_v(\nabla_{\boldsymbol{y}}\boldsymbol{h}_v)^T\rangle_{\Omega_v}I\quad\text{and}\quad \hat{\bar{K}}_m(\omega)=\hat{\bar{K}}_m(\omega)I=\frac{d^2}{\mu}\langle\hat{Q}_m(\boldsymbol{y},\omega)\rangle_{\Omega_m}I. \tag{6.1}$$

For the solution of the cell problem in the phase Ω_v, we refer to [1, appendix C]. For the phase Ω_m, we solve the problem (3.41) with $\alpha=1$ using the steady Brinkman equation module in COMSOL Multiphysics. We use the PARDISO solver and the $\mathbb{P}_2^3-\mathbb{P}_1$ finite-element discretization for the velocity and the pressure, respectively. Moreover, we perform a parametric sweep analysis varying ω to obtain the solution for different frequencies. After that, we apply the average operator to obtain $\langle\hat{Q}_m(\boldsymbol{y},\omega)\rangle_{\Omega_m}$. We obtain the dimensional hydraulic conductivity $\hat{\bar{K}}_m(\omega)$ shown in figure 2.

If we take the values of the permeability $\langle\hat{Q}_m(\boldsymbol{y},\omega)\rangle_{\Omega_m}$ and we perform an inverse Fourier transform (with the MATLAB built-in command *ifft*), we find the dimensional average hydraulic conductivity shown in figure 3. As expected, we have a permeability that decreases in time [8]. The decreasing imaginary part of $\langle\hat{Q}_m(\boldsymbol{y},\omega)\rangle_{\Omega_m}$ in figure 2 is connected to the decrease in time of the permeability (due to the memory effect of the macroscopic Darcy's Law). If we compare the ifft result with the solution of the cell problem (3.45), we have a maximum relative error of 0.188%. Moreover, we have that the real part of the permeability is similar to the one found in the steady case in [1]. We believe these values to be realistic because, at time zero, we have the same permeability values we found in the steady setting [1]. Additionally, as time increases, the permeability tends to zero very fast, reflecting its

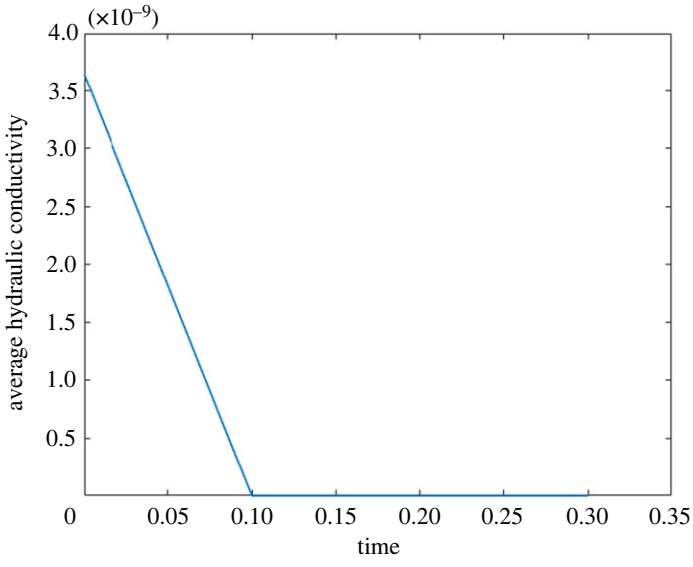

Figure 3. The inverse Fourier transform of the dimensional average hydraulic conductivity in $mm^3\,s\,mg^{-1}$ calculated numerically using the command ifft to the solution plot in figure 2 with physiological values of the lymph node (table 1).

diminishing influence on the flow dynamics at the time we are studying our flow, a characteristic commonly observed in memory-type equations [8].

To study in more detail the mesh of the previous solution, we perform an adaptive mesh refinement study. After this process, we compare the two $\hat{\bar{K}}_m(\omega)$ that we found, and we obtain, for all the values of ω, a maximum relative error of 0.06%.

To test the Brinkman equation module in Comsol with complex numbers, we run some simulations in a cylindrical geometry and we compare the solution to the following explicit solution (found in [1]):

$$W^{DB}_{33,v}(r) = K^*\left[1 - \frac{J_0\big(i\sqrt{(1/\mu^* K^*)}r\big)}{J_0\big(i\sqrt{(1/\mu^* K^*)}\hat{r}_c\big)}\right], \quad W^{DB}_{31,v} = W^{DB}_{32,v} = 0.$$

Taking the average, we obtain

$$\langle W^{DB}_{33,v}\rangle_{\Omega_v} = \frac{2\pi l_c}{|\Omega_{\text{cyl}}|}K^*\left[\frac{\hat{r}_c^2}{2} + i\sqrt{\mu^* K^*}\hat{r}_c\frac{J_1\big(i\sqrt{(1/\mu^* K^*)}\hat{r}_c\big)}{J_0\big(i\sqrt{(1/\mu^* K^*)}\hat{r}_c\big)}\right], \tag{6.2}$$

where l_c is the cylinder length, Ω_{cyl} is the cylinder volume, K^* is the permeability, $\hat{r}_c$ is the cylinder radius, μ^* is the viscosity, J_0 and J_1 are the Bessel functions of the first and second kind, respectively. We run the numerical simulations and compare the solution to the explicit one (6.2) with the following (non-dimensional) data: $l_c = 1$, $\hat{r}_c = 7.7 \times 10^{-3}$, $K^* = 6.66 \times 10^{-6} + i$, $6.66 \times 10^{-6} + 10i$, $6.66 \times 10^{-6} + 100i$, $\mu^* = 1$. We found that the maximum relative error between the numerical and the explicit solution is 0.67% for the real part and 1.9% for the imaginary part.

7. Study of the fluid flow in a lymph node

In this section, we study the fluid flow inside the lymph node using the model results obtained in the previous sections of this work. In particular, we use the explicit solution of §5 applied to the porous region of the node (the LC) because all the lymph node vascularization is situated in this region [47–49]. Moreover, we assume that the lymph node has a spherical shape, and we use physiological lymph node data inspired by a mouse popliteal lymph node [1,47,59]. The explicit solution of §5 is implemented in MATLAB. To compute the inverse Fourier transform, we use the MATLAB built-in command *ifft*, that is, the *inverse fast Fourier transform*.

We have that Ω_v and Ω_m are the portions of the domain that represent the blood vessels and the FRC network, respectively. Choosing $\bar{p}(t) = \sigma(\pi_m(t) - \pi_v(t))$, we describe the fluid exchange between the phases mentioned above using the well-known Starling equation [62,63]. Moreover, all the physiological data used are summarized in table 1, and the meaning of these data is explained in [1, appendix B].

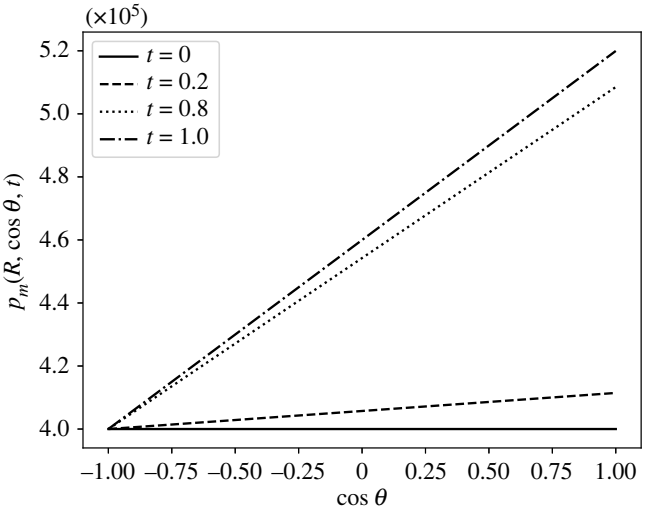

Figure 4. The pressure distribution in mPa of equation (7.1) calculated at different times (in seconds).

As we can see from the previous sections, here the hydraulic conductivity of the phase Ω_m depends on time due to the memory term in the Darcy equation (4.1). This is very different from the previous works on the lymph node [1,47,53,54,57–59], as it allows for a comprehensive analysis of the lymph's time behaviour through a rigorous homogenization method.

Using physiological data obtained from the literature on the lymph node, we find that the parameter that governs the time dependency of our problem is $\eta \approx 0.1$, in line with the Womersley number found in the lymphatic system [36].

At the boundary, we have the following boundary conditions:

$$p_m(R, \zeta, t) = \bar{p}_m(\zeta, t) \quad \text{and} \quad p_v(R, \zeta, t) = \bar{p}_v,$$

where $\bar{p}_m(\zeta, t)$ is a general function in ζ and t, and $\bar{p}_v$ is the mean of the blood vessel pressure data (in general constant).

As we mentioned in [1], the variation with respect to $\zeta = \cos\theta$ of the boundary condition $\bar{p}_m$ is essential to mimic the pressure distribution in the SCS. The precise pressure distribution of the SCS is not well known so, to circumvent this lack of data in the literature and inspired by [45], we take a linear relation between the pressure and $\zeta = \cos\theta$. This linear relation connects the maximum value of the pressure $\bar{p}_{m,\max} = 3.9\,\text{mmHg} \approx 5.2 \times 10^5\,\text{mPa}$ with the minimum value of $\bar{p}_{m,\min} = 3\,\text{mmHg} \approx 4 \times 10^5\,\text{mPa}$, taken from the numerical results of [47]. Moreover, to describe the pulsatile inflow, we take a pressure distribution that varies over time in the following way:

$$\bar{p}_m(\zeta, t) = \bar{p}_{m,\min} + \frac{1}{2}(1 - \cos(\pi t))\frac{\zeta + 1}{2}(\bar{p}_{m,\max} - \bar{p}_{m,\min}). \tag{7.1}$$

We can see the behaviour of the boundary condition (7.1) with respect to ζ at different times in figure 4.

We use the following physiological parameters: $\sigma = 0.88$, $\pi_v - \pi_m = 1.02 \times 10^6$ mPa, $L_p = 5.475 \times 10^{-10}\,\text{mm}\,\text{s}^{-1}\,\text{mPa}^{-1}$ and $\bar{p}_v = 6.66 \times 10^5$. We can see the behaviour of the interstitial pressure p_m over time in figure 5. As we can see, the minimum of the interstitial pressure p_m increases and moves from the centre of the node to the lower part of the node. This is due to the fact that, as time passes, the boundary pressure distribution (7.1) remains linear but the maximum of the pressure increases, and this effect combines with the effect of the fluid exchange between phases. This phenomenon highlights the importance of the time dependency of the flow inside the node. We note that the Darcy equation linearly relates the fluid discharge to the pressure gradient, so the lymph moves accordingly to the pressure, which means that a sink term is represented by a lower pressure region in the node.

As expected and in accordance with [1], increasing L_p results in a decrease of p_m and an increase of p_v at the centre of the node. We can see this behaviour of the interstitial pressure p_m in the contour plot of figure 6 at time $t = 1$ s. As we can see, the results are in line with the steady one [1], which means that the increase of L_p decreases and moves the minimum of p_m towards the centre of the node.

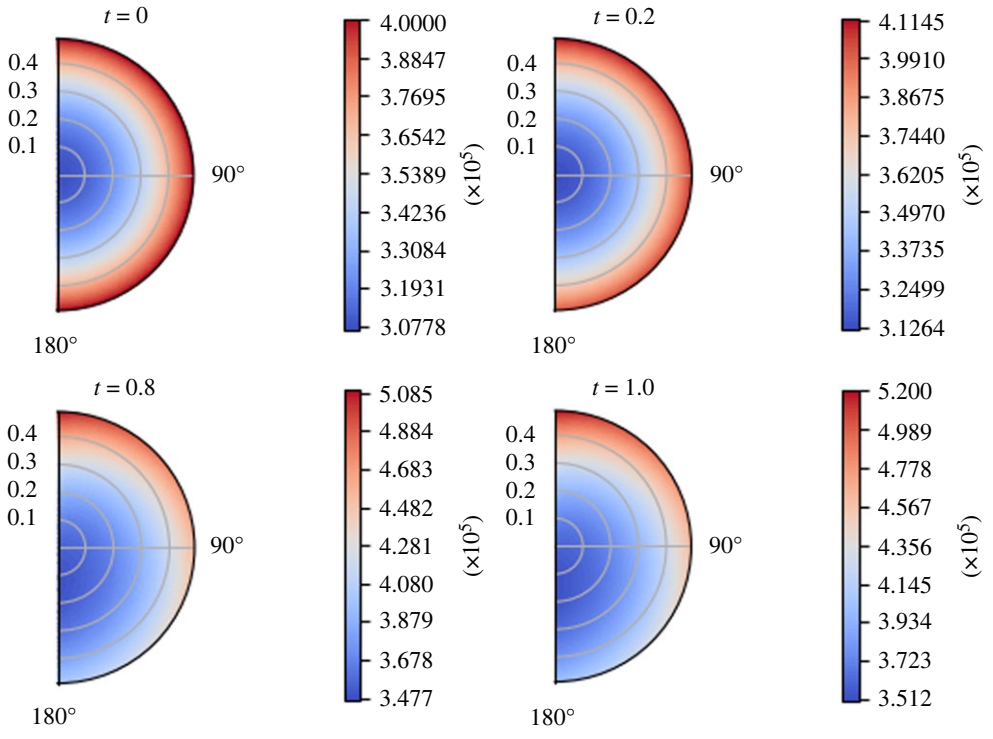

Figure 5. The variation of the interstitial pressure p_m (in mPa) with respect to time (in seconds), with the parameters in table 1 and $\pi_v - \pi_m = 1.02 \times 10^6$ mPa, $L_p = 5.475 \times 10^{-10}$ mm s^{-1} mPa^{-1}, $\bar{p}_v = 6.66 \times 10^5$ mPa and the boundary conditions (7.1).

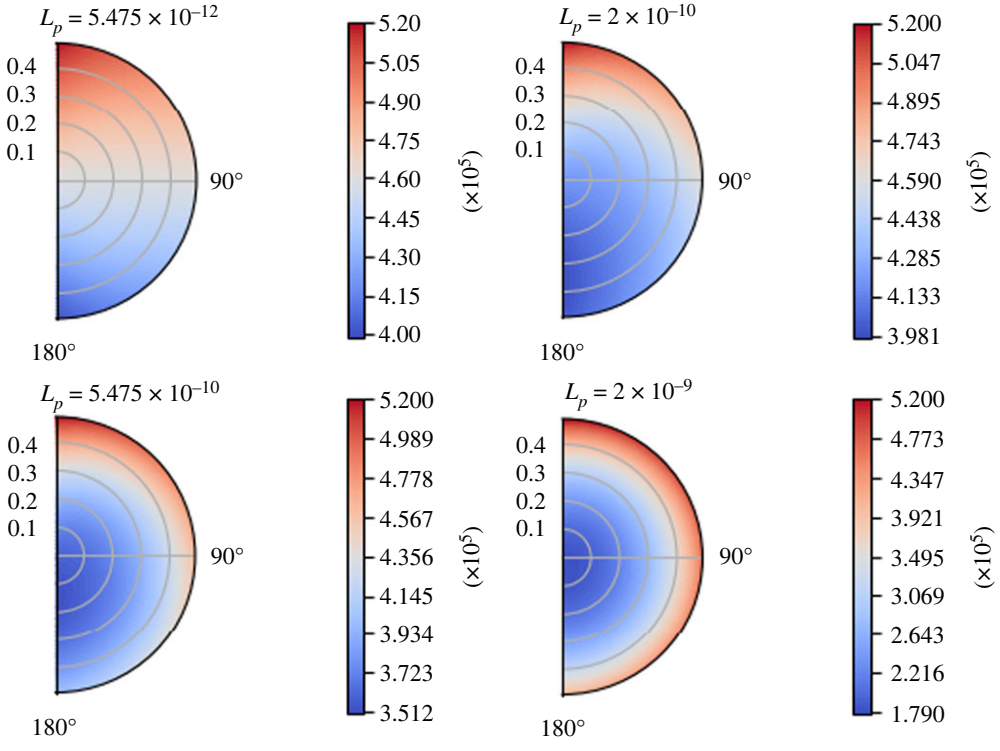

Figure 6. The variation of the interstitial pressure p_m (in mPa) varying L_p (in mm s^{-1} mPa^{-1}) at time $t = 1$ s, with the parameters in table 1, $\pi_v - \pi_m = 1.02 \times 10^6$ mPa, $\bar{p}_v = 6.66 \times 10^5$ mPa and the boundary conditions (7.1).

In figures 7 and 8, one can see the behaviour of the interstitial pressure p_m and the blood vessel pressure p_v for some values of $\bar{p}_v$ at time $t = 1$ s. When $\bar{p}_v$ increases, we have the opposite behaviour of the one found for L_p: the minimum value of the interstitial pressure p_m moves towards the lower

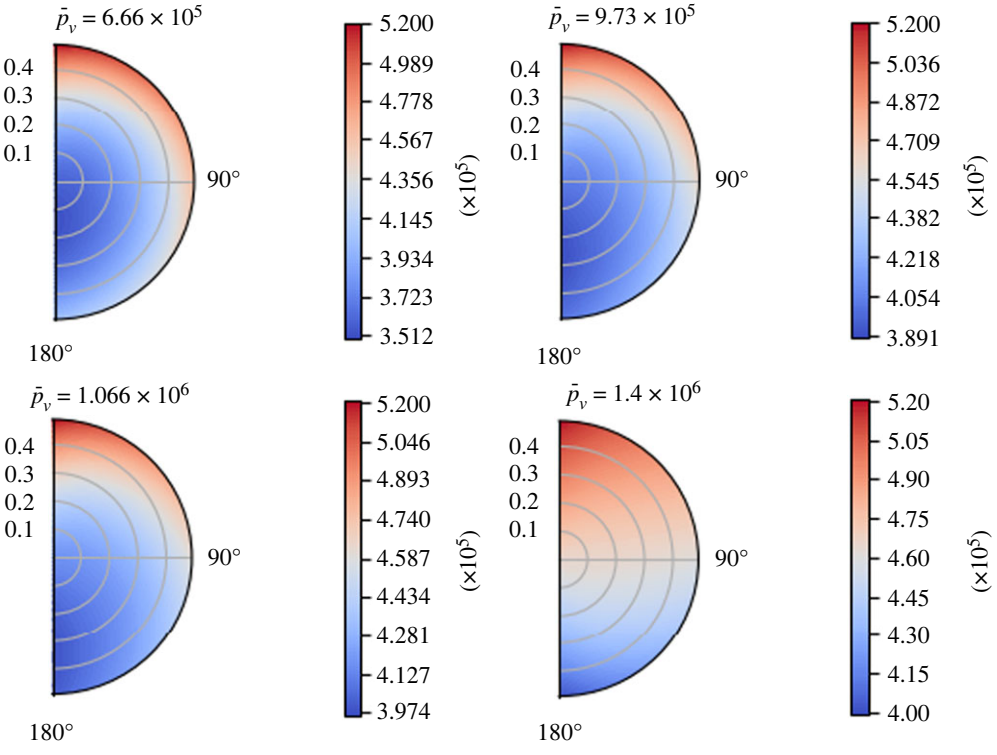

Figure 7. The variation of the interstitial pressure p_m (in mPa) varying the mean blood vessel pressure $\bar{p}_v$ (in mPa) at time $t = 1$ s, with the parameters in table 1, $\pi_v - \pi_m = 1.02 \times 10^6$ mPa, $L_p = 5.475 \times 10^{-10}$ mm s^{-1} mPa^{-1} and the boundary conditions (7.1).

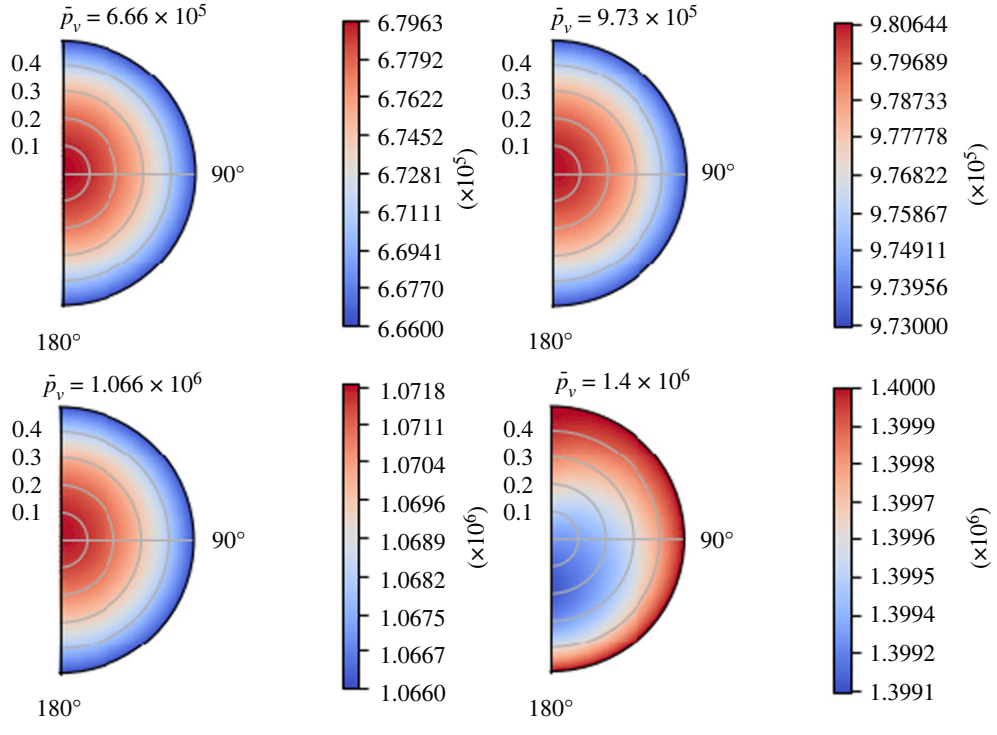

Figure 8. The variation of the blood vessel pressure p_v (in mPa) for some values of the mean blood vessel pressure $\bar{p}_v$ (in mPa) at time $t = 1$ s, with the parameters in table 1, $\pi_v - \pi_m = 1.02 \times 10^6$ mPa, $L_p = 5.475 \times 10^{-10}$ mm s^{-1} mPa^{-1} and the boundary conditions (7.1).

part of the node and the fluid exchange between the two phases decreases (because the minimum of p_m increases); on the contrary, the maximum of the blood vessel pressure p_v increases. We have an inversion of the flow direction for every t at $\bar{p}_v \approx 1.4$ mPa ≈ 10.5 mmHg, which is the same value found in [47] and

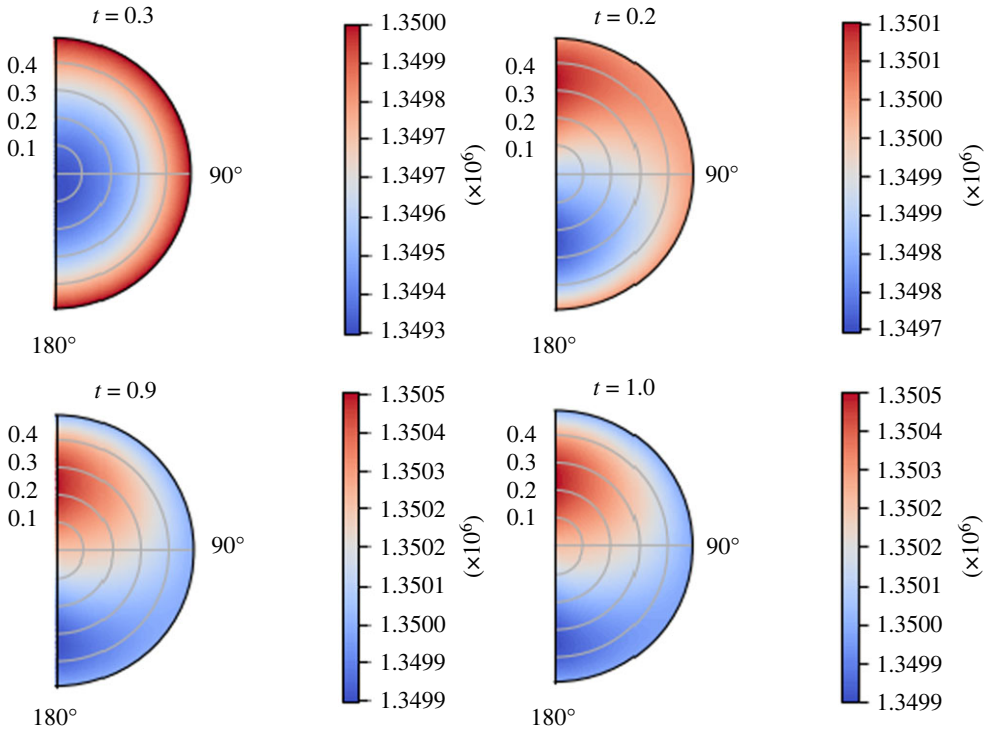

Figure 9. The variation of the blood vessel pressure distribution p_v (in mPa) with respect to time (in seconds), with the parameters in table 1, $\pi_v - \pi_m = 1.02 \times 10^6$ mPa, $\bar{p}_v = 1.35 \times 10^6$ mPa, $L_p = 5.475 \times 10^{-10}$ mm s^{-1} mPa^{-1} and the boundary conditions (7.1).

in [1]; from this value to higher values of $\bar{p}_v$, the maximum of p_m starts to move towards the centre of the node. This behaviour is in accordance with the findings in [1]. Moreover, we can have flow inversion for only certain values of the time; for instance, we can see figure 9, where we plot the blood vessel pressure p_v at different times with $\bar{p}_v = 1.35 \times 10^6$ mPa. For the initial times, we have a flow inversion, which means that the fluid moves from phase Ω_v to phase Ω_m, resulting in a region of minimum pressure at the centre of the node for p_v. As time passes, the boundary condition (7.1) increases the pressure in the upper region of the lymph node (near $\theta = 0$), and this results in a region of higher pressure zone near $\theta = 0$ and the region of lower pressure zone moves near $\theta = \pi$.

Increasing $\Delta\pi$ means an increase in the concentration difference between the blood vessels and the FRC phase, and this results in a decrease of the minimum of p_m and moves it to the centre of the node, and an increase of the maximum of p_v. We can see a contour plot of p_m at $t = 1$ s varying $\Delta\pi$ in figure 10.

From the fact that the boundary condition $\bar{p}_m(\zeta, t)$ can be chosen as we want, we solve our explicit solution using the solution we found in our previous paper [59] using the stream function approach. We refer to [59] for more details about the computations and the data of this pressure distribution; this solution is calculated in a div-free setting, where we fix $\bar{p}_m(R_2, -1) = 6.18 \times 10^5$ mPa and with a time pulsation of the form $(1 - \cos(\pi t))/2$. In figure 11, we can see the boundary pressure distribution. The fast increment near $\zeta = 1$ represents the inlet condition, and the fast decrement near $\zeta = -1$ represents the outlet condition. In figures 12 and 13, we can see the pressure and the velocity distribution over time using the parameters $\bar{p}_v = 1.06 \times 10^6$ mPa, $\pi_v - \pi_m = 1.02 \times 10^6$ mPa, $L_p = 5.475 \times 10^{-11}$ mm s^{-1} mPa^{-1}, and the above-mentioned boundary pressure. As we can see, for initial times, we have a similar pressure distribution to that we found in the previous case but, as time passes, it becomes more evident the higher pressure near the inlet and the lower pressure near the outlet. We can see this behaviour for the velocity magnitude too, where at $t = 1$ s, we can see a higher difference between the inlet–outlet velocity and the velocity at the centre of the node.

Moreover, we have that the velocities that we found inside the LC are in agreement with the literature [47,55,79–81]. We found a higher velocity (at time $t = 1$ s) with respect to the steady case [1]; moreover, we have that the pressure change (at time $t = 1$ s) between the upper region (near the inlet condition) and the lower region (near the outlet condition) is higher here too.

Finally, we have performed a parameter sensitivity analysis and found that on varying the average hydraulic conductivity, the resulting pressure (interstitial and blood pressure) exhibits only a relatively

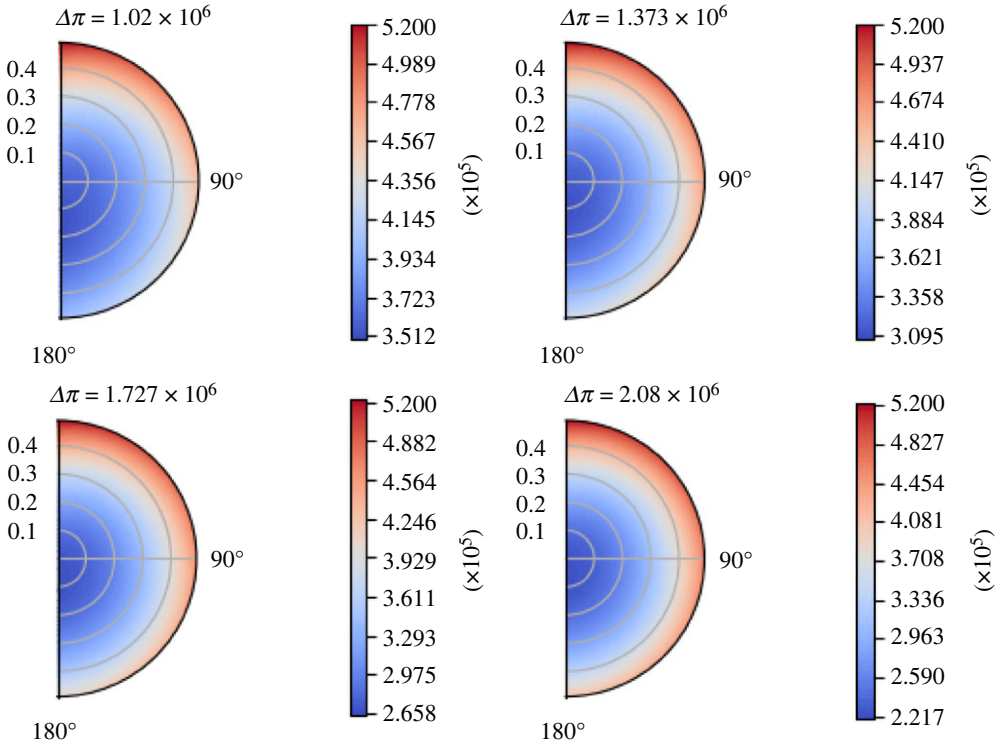

Figure 10. The variation of the interstitial pressure p_m (in mPa) varying $\Delta\pi$ (in mPa), with the parameters in table 1, $\bar{p}_v = 6.66 \times 10^5$ mPa, $L_p = 5.475 \times 10^{-10}$ mm s^{-1} mPa^{-1}, and the boundary conditions (7.1).

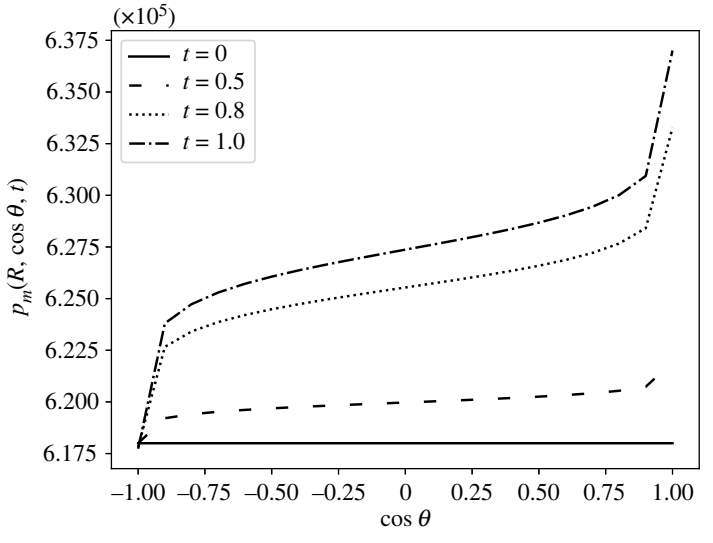

Figure 11. The variation of the interstitial pressure p_m (in mPa) calculated at the boundary (using the computations of [59]) with respect to $\zeta = \cos\theta$ at different times (in seconds), with the parameters in table 1, $\Delta\pi = 1.02 \times 10^6$ mPa, $L_p = 5.475 \times 10^{-11}$ mm s^{-1} mPa^{-1} and $\bar{p}_v = 1.06 \times 10^6$ mPa.

small variation. In particular, a variation of 1, 2, and 5% of the average hydraulic conductivity corresponds to the relative variations of the interstitial pressure of 0.012, 0.0238 and 0.0578%.

8. Conclusion

In this paper, we use the asymptotic homogenization technique in a time-dependent setting, starting from the equations and interface conditions (2.1), (2.2), (2.4), assuming both local periodicity and macroscopic uniformity.

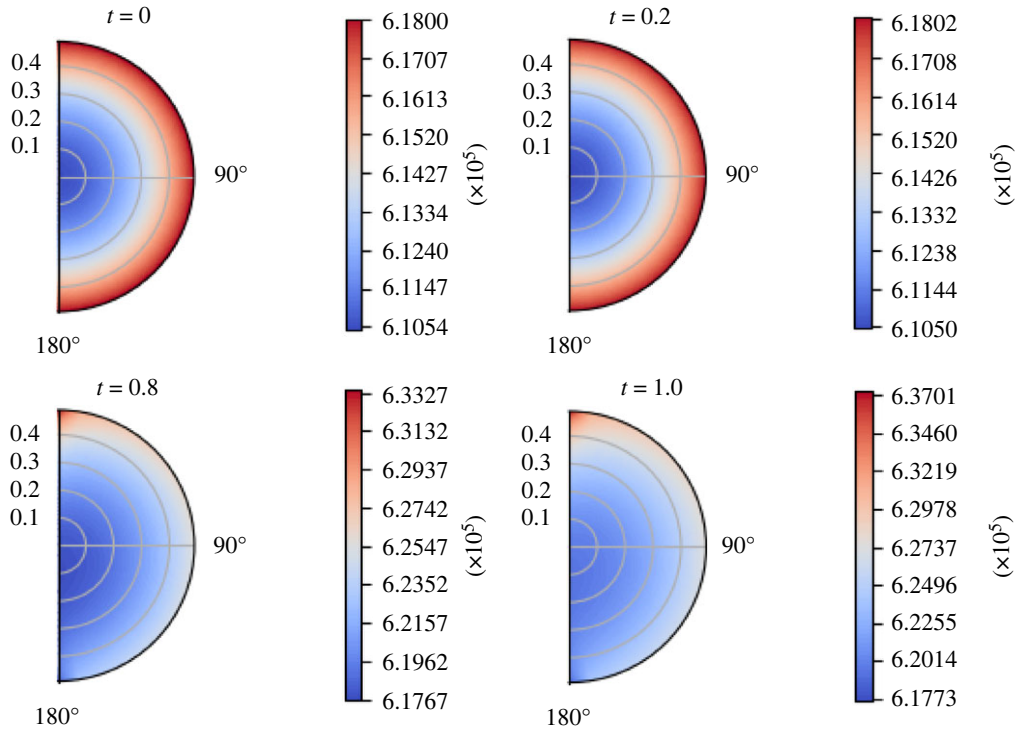

Figure 12. The variation of p_m (in mPa) with respect to time (in seconds) with the boundary pressure shown in figure 11, $\Delta\pi = 1.02 \times 10^6$ mPa, $L_p = 5.475 \times 10^{-11}$ mm s^{-1} mPa^{-1}, $\bar{p}_v = 1.06 \times 10^6$ mPa and the parameters in table 1.

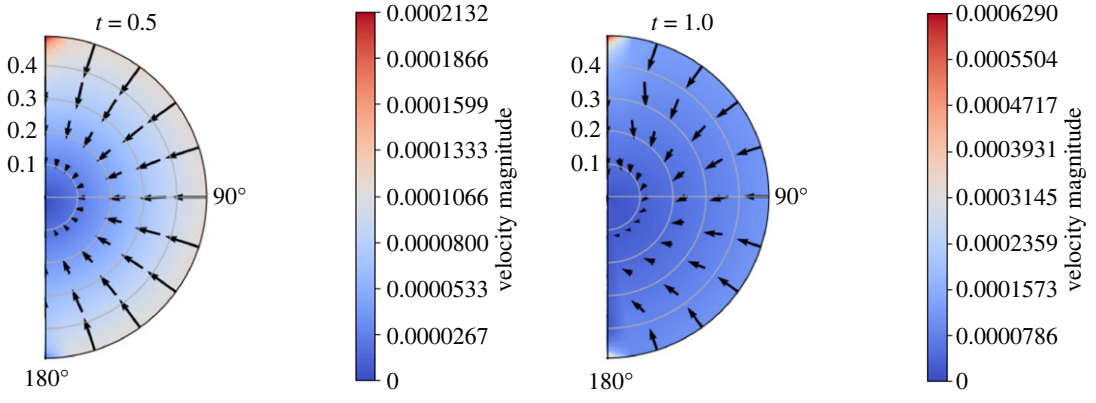

Figure 13. The contour plot of the velocity of the phase Ω_m (in mm s^{-1}) with respect to time (in seconds) with the boundary pressure shown in figure 11, $\Delta\pi = 1.02 \times 10^6$ mPa, $L_p = 5.475 \times 10^{-11}$ mm s^{-1} mPa^{-1}, $\bar{p}_v = 1.06 \times 10^6$ mPa and the parameters in table 1.

This model is a non-trivial extension of our previous model [1]; here, we have considered a time-dependent Darcy–Brinkman equation, which results in a Darcy equation with memory at the macroscale for the phase Ω_m. The time dependency is considered for the pulsation behaviour of the lymph [36,37,61,82] and allows us to study the fluid behaviour inside the lymph node in more detail [39,40,59]. With lymph node physiological data, the characteristic time is $\eta \approx 0.1$: this is in agreement with the Womersley number found for the lymphatic system [36].

This model has been designed to be applied to the flow of lymph within the lymph node, but the derivation of the model has been intentionally kept as general as possible to be applicable to other problems as well.

After the derivation of the macroscopic equations that described the time-dependent fluid flow (§4), in §5, we have found the explicit solution of the proposed model in a spherical domain, using the computations of the solution that we found in [1] and the properties of the Fourier transform. Subsequently, we have studied the fluid and pressure distribution within the lymph node using the

above-mentioned explicit solution and physiological data inspired by an idealized spherical mouse popliteal lymph node. Incorporating the temporal component into the proposed model has allowed us to study how lymph pulsations influence these quantities within a lymph node. Regarding this multiscale formulation, our primary focus has been directed towards the porous region of the lymph node (the LC). Moreover, we have placed particular emphasis on studying the fluid exchange that occurs between the interstitial space of the lymph node and the blood vessels, which are exclusively present in this specific part of the node [47–49]. We have analysed how various parameters influence fluid absorption and pressure (i.e. velocity) over time, and the obtained results align with findings documented in the literature [1,47,73–75,83].

Let us now explore considerations that could enhance the model in the future. In this work, we solely focused on the LC, but it would be interesting to couple this model with the fluid flow in the SCS to describe the fluid flow in the entire lymph node.

The Beavers–Joseph–Saffman interface condition (2.4) used in this work is initially established in a two-dimensional setting, and expanding it to three dimensions presents a significant and complex challenge [2,84–88]. Moreover, it would be interesting to study how the physico-chemical properties of the interface affect the solution [67].

When we applied our model to the lymph node, we assumed negligible forces to simplify our model and due to a lack of data regarding them in the literature. However, it is important to note that in practical situations, such forces can play a significant role, especially when using electromagnetic fields, as seen in [89,90] within the context of cancer hyperthermia. Hence, when we have access to physiological data, it becomes crucial to account for the impact of inhomogeneous volume loads, as discussed in [24]. We can say the same for the velocity initial condition, which we have assumed to be zero. In general, we can have more general fluid behaviour as an initial condition, in particular in drug delivery applications [25].

In our model, we have taken into account the time variation of the concentration of protein inside the node, but we have supposed it to be constant due to a lack of precise data. Incorporating the temporal and spatial behaviour of protein concentration, as discussed in [3], and together with physiological data, would be a compelling and valuable direction to explore.

In this work, we have assumed a rigid porous matrix to keep the model as simple as possible and due to the lack of biological data regarding this problem; a possible extension of this model is to take into account a deformable matrix that interacts with the lymph flow inside the node, for example by considering the modelling framework developed in [91,92].

Finally, due to our explicit analysis, we assumed a spherical lymph node. In general, lymph nodes have a more complex geometry, typically an ellipsoid shape [47,53,54]. If we can access more realistic data regarding their shape through medical imaging [53,54], our model could be used for more realistic numerical simulations to make physiologically meaningful predictions in the future.

Ethics. This work did not require ethical approval from a human subject or animal welfare committee.

Data accessibility. This article has no additional data.

Declaration of AI use. We have not used AI-assisted technologies in creating this article.

Authors' contributions. A.G.: data curation, formal analysis, investigation, methodology, writing—original draft, writing—review and editing; G.G.: conceptualization, investigation, project administration, supervision, writing—review and editing; A.M.: conceptualization, investigation, methodology, writing—review and editing; R.P.: conceptualization, investigation, methodology, project administration, supervision, writing—review and editing.

All authors gave final approval for publication and agreed to be held accountable for the work performed therein.

Conflict of interest declaration. We declare we have no competing interests.

Funding. This work was partially supported by National Group of Mathematical Physics (GNFM-INdAM). R.P. is partially funded by EPSRC grant nos. EP/S030875/1 and EP/T017899/1. Project funded by the European Union—Next Generation EU under the National Recovery and Resilience Plan (NRRP), Mission 4 Component 2 Investment 1.1—Call PRIN 2022 no. 104 of 2 February 2022 of Italian Ministry of University and Research; Project 202249PF73 (subject area: PE–Physical Sciences and Engineering) 'Mathematical models for viscoelastic biological matter'.

References

1. Girelli A, Giantesio G, Musesti A, Penta R. 2023 Effective governing equations for dual porosity Darcy-Brinkman systems subjected to inhomogeneous body forces and their application to the lymph node. *Proc. R. Soc. A* **479**, 20230137. (doi:10.1098/rspa.2023.0137)
2. Shipley RJ, Chapman SJ. 2010 Multiscale modelling of fluid and drug transport in vascular tumours. *Bull. Math. Biol.* **72**, 1464–1491. (doi:10.1007/s11538-010-9504-9)
3. Penta R, Ambrosi D, Quarteroni A. 2015 Multiscale homogenization for fluid and drug transport in vascularized malignant tissues. *Math. Models Methods Appl. Sci.* **25**, 79–108. (doi:10.1142/S0218202515500037)

4. Arbogast T, Douglas JJ, Hornung U. 1990 Derivation of the double porosity model of single phase flow via homogenization theory. *SIAM J. Math. Anal.* **21**, 823–836. (doi:10.1137/052104)
5. Auriault JL, Boutin C. 1992 Deformable porous media with double porosity. Quasi-statics. I. Coupling effects. *Transp. Porous Media* **7**, 63–82. (doi:10.1007/BF00617317)
6. Auriault JL, Boutin C. 1993 Deformable porous media with double porosity. Quasi-statics. II. Memory effects. *Transp. Porous Media* **10**, 153–169. (doi:10.1007/BF00617006)
7. Rohan E, Turjanicovà J, Lukeš V. 2018 A Darcy–Brinkman model of flow in double porous media: two-level homogenization and computational modelling. *Comput. Struct.* **207**, 95–110. (doi:10.1016/j.compstruc.2017.08.006)
8. Hornung U. 1997 *Homogenization and porous media*. New York, NY: Springer.
9. Gerisch A, Penta R, Lang J. 2018 *Multiscale models in mechano and tumor biology*. Cham, Switzerland: Springer.
10. Brinkman H. 1949 A calculation of the viscous force exerted by a flowing fluid on a dense swarm of particles. *Appl. Sci. Res.* **A1**, 27–34. (doi:10.1007/BF02120313)
11. Darcy H. 1856 *Les fontaines publiques de la ville de Dijon*. Paris, France: Victor Dalmont.
12. Rajagopal KR. 2007 On a hierarchy of approximate models for flows of incompressible fluids through porous solids. *Math. Models Methods Appl. Sci.* **17**, 215–252. (doi:10.1142/S0218202507001899)
13. Auriault JL, Geindreau C, Boutin C. 2005 Filtration law in porous media with poor separation of scales. *Transp. Porous Media* **60**, 89–108. (doi:10.1007/s11242-004-3649-7)
14. Lévy T. 1983 Fluid flow through an array of fixed particles. *Int. J. Eng. Sci.* **21**, 11–23. (doi:10.1016/0020-7225(83)90035-6)
15. Hill A, Straughan B. 2008 Poiseuille flow in a fluid overlying a porous medium. *J. Fluid Mech.* **603**, 137–149. (doi:10.1017/S0022112008000852)
16. Brillard A. 1986–1987 Asymptotic analysis of incompressible and viscous fluid flow through porous media. Brinkman's law via epi-convergence methods. *Ann. de la Faculté des sciences de Toulouse: Math.* **8**, 225–252.
17. Allaire G. 1991 Homogenization of the Navier-Stokes equations in open sets perforated with tiny holes I. Abstract framework, a volume distribution of holes. *Arch. Ration. Mech. Anal.* **113**, 209–259. (doi:10.1007/BF00375065)
18. Allaire G. 1991 Homogenization of the Navier-Stokes equations in open sets perforated with tiny holes II. Non-critical sizes of the holes for a volume distribution and a surface distribution of holes. *Arch. Ration. Mech. Anal.* **113**, 261–298. (doi:10.1007/BF00375066)
19. Auriault JL. 2009 On the domain of validity of Brinkman's equation. *Transp. Porous Med.* **79**, 215–223. (doi:10.1007/s11242-008-9308-7)
20. Marusic-Paloka E, Pazanin I, Marusic S. 2012 Comparison between Darcy and Brinkman laws in a fracture. *Appl. Math. Comput.* **218**, 7538–7545. (doi:10.1016/j.amc.2012.01.021)
21. Naele G, Nader W. 1974 Practical significance of Brinkman's extension of Darcy's law: coupled parallel flows within a channel and a bounding porous medium. *Can. J. Chem. Eng.* **52**, 475–478. (doi:10.1002/cjce.5450520407)
22. Vuong AT, Yoshihara L, Wall WA. 2014 A general approach for modeling interacting flow through porous media under finite deformations. *Comput. Methods Appl. Mech. Eng.* **283**, 1240–1259. (doi:10.1016/j.cma.2014.08.018)
23. Bear J, Bachmat Y. 1990 *Introduction to modelling of transport phenomena in porous media*. Dordrecht, The Netherlands: Kluwer.
24. Penta R, Ramìrez-Torres AD, Merodio J, Rodríguez-Ramos R. 2020 Effective governing equations for heterogenous porous media subject to inhomogeneous body forces. *Math. Eng.* **3**, 1–17. (doi:10.3934/mine.2021033)
25. Netti PA, Baxter LT, Boucher Y, Skalak R, Jain RK. 1995 Time-dependent behavior of interstitial fluid pressure in solid tumors: implications for drug delivery. *Cancer Res.* **55**, 5451–5458.
26. Mikelić A. 1994 Mathematical derivation of the Darcy-type law with memory effects, governing transient flow through porous media. *Glasnik Matematicki* **29**, 57–77.
27. Lions JL. 1981 *Some methods in the mathematical analysis of systems and their control*. New York, NY: Science Press.
28. Burridge R, Keller JB. 1981 Poroelasticity equations derived from microstructure. *J. Acoust. Soc. Am.* **70**, 1140–1146. (doi:10.1121/1.386945)
29. Lasseux D, Valdés-Parada FJ, Bellet F. 2019 Macroscopic model for unsteady flow in porous media. *J. Fluid Mech.* **862**, 283–311. (doi:10.1017/jfm.2018.878)
30. Tartar L. 1990 Memory effects and homogenization. *Arch. Ration. Mech. Anal.* **111**, 121–133. (doi:10.1007/BF00375404)
31. Tartar L. 1989 Nonlocal effects induced by homogenization. In *Partial differential equations and the calculus of variations* (eds F Colombini, A Marino, L Modica, S Spagnolo), pp. 925–938. Boston, MA: Birkhäuser. (doi:10.1007/978-1-4615-9831-2_19)
32. Mozokhina A, Savinkov R. 2020 Mathematical modelling of the structure and function of the lymphatic system. *Mathematics* **8**, 1467. (doi:10.3390/math8091467)
33. Margaris KN, Black RA. 2012 Modelling the lymphatic system: challenges and opportunities. *J. R. Soc. Interface* **9**, 601–612. (doi:10.1098/rsif.2011.07511)
34. Caulk AW, Nepiyushchikh ZV, Shaw R, Dixon JB. 2015 Quantification of the passive and active biaxial mechanical behaviour and microstructural organization of rat thoracic ducts. *J. R. Soc. Interface* **12**, 20150280. (doi:10.1098/rsif.2015.0280)
35. Caulk AW, Dixon JB, Gleason J.RL. 2016 A lumped parameter model of mechanically mediated acute and long-term adaptations of contractility and geometry in lymphatics for characterization of lymphedema. *J. Physiol.* **15**, 1601–1618. (doi:10.1007/s10237-016-0785-2)
36. Moore Jr JE, Bertram CD. 2018 Lymphatic system flows. *Annu. Rev. Fluid Mech.* **50**, 459–482. (doi:10.1146/annurev-fluid-122316-045259)
37. Bertram CD, Macaskill C, Davis MJ, Moore J.JE. 2017 Valve-related modes of pump failure in collecting lymphatics: numerical and experimental investigation. *Biomech. Model. Mechanobiol.* **16**, 1987–2003. (doi:10.1007/s10237-017-0933-3)
38. Bertram CD, Macaskill C, Moore J.JE. 2019 Inhibition of contraction strength and frequency by wall shear stress in a single-lymphangion model. *J. Biomech. Eng.* **141**, 111006. (doi:10.1115/1.4043724)
39. Birmingham KG, O'Melia MJ, Bordy S, Aguilar DR, El-Reyas B, Lesinski G, Thomas SN. 2020 Lymph node subcapsular sinus microenvironment-on-a-chip modeling shear flow relevant to lymphatic metastasis and immune cell homing. *iScience* **23**, 101751. (doi:10.1016/j.isci.2020.101751)
40. O'Melia MJ, Lund AW, Thomas SN. 2019 The biophysics of lymphatic transport: engineering tools and immunological consequences. *iScience* **22**, 28–43. (doi:10.1016/j.isci.2019.11.005)
41. Arasa J, Collado-Diaz V, Halin C. 2021 Structure and immune function of afferent lymphatics and their mechanistic contribution to dendritic cell and T cell trafficking. *Cells* **10**, 1269. (doi:10.3390/cells10051269)
42. Apoorva F *et al.* 2018 How biophysical forces regulate human B cell lymphomas. *Cell Rep.* **23**, 499–511. (doi:10.1016/j.celrep.2018.03.069)
43. Tobbia D, Semple J, Baker A, Dumont D, Semple A, Johnston M. 2009 Lymphedema development and lymphatic function following lymph node excision in sheep. *J. Vasc. Res.* **46**, 426–434. (doi:10.1159/000194273)
44. Novkovic M, Onder L, Bocharov G, Ludewig B. 2020 Topological structure and robustness of the lymph node conduit system. *Cell Rep.* **30**, 893–904. (doi:10.1016/j.celrep.2019.12.070)
45. Grebennikov D, Van Loon R, Novkovic M, Onder L, Savinkov R, Sazonov I, Tretyakova R, Watson DJ, Bocharov G. 2016 Critical issues in modelling lymph node physiology. *Computation* **5**, 3. (doi:10.3390/computation5010003)
46. Savinkov R, Kislitsyn A, Watson DJ, van Loon R, Sazonov I, Novkovic M, Onder L, Bocharov G. 2017 Data-driven modelling of the FRC network for studying the fluid flow in the conduit system. *Eng. Appl. Artif. Intell.* **62**, 341–349. (doi:10.1016/j.engappai.2016.10.007)
47. Jafarnejad M, Woodruff MC, Zawieja DC, Carroll MC, Moore Jr JE. 2015 Modeling lymph flow and fluid exchange with blood vessels in lymph nodes. *Lymphat. Res. Biol.* **13**, 234–247. (doi:10.1089/lrb.2015.0028)

48. Jafarnejad M, Ismail AZ, Duarte D, Vyas C, Ghahramani A, Zawieja DC, Lo Celso C, Poologasundarampillai G, Moore Jr JE. 2019 Quantification of the whole lymph node vasculature based on tomography of the vessel corrosion casts. *Nat. Sci. Rep.* **9**, 13380. (doi:10.1038/s41598-019-49055-7)
49. Kelch ID, Bogle G, Sands GB, Phillips ARJ, LeGrice IJ, Dunbar PR. 2015 Organ-wide 3D-imaging and topological analysis of the continuous microvascular network in a murine lymph node. *Nat. Sci. Rep.* **16**, 16534. (doi:10.1038/srep16534)
50. Jayathungage Don TD, Safaei S, Maso Talou GD, Russell PS, Phillips ARJ, Reynolds HM. 2023 Computational fluid dynamic modeling of the lymphatic system: a review of existing models and future directions. *Biomech. Model. Mechanobiol.* **23**, 3–22. (doi:10.1007/s10237-023-01780-9)
51. Novkovic M, Onder L, Cheng HW, Bocharov G, Ludewig B. 2018 Integrative computational modeling of the lymph node stromal cell landscape. *Front. Immunol.* **9**, 2428. (doi:10.3389/fimmu.2018.02428)
52. Shanti A, Teo J, Stefanini C. 2018 In vitro immune organs-on-chip for drug development: a review. *Pharmaceutics* **10**, 278. (doi:10.3390/pharmaceutics10040278)
53. Cooper LJ, Heppell JP, Clough GF, Ganapathisubramani B, Roose T. 2016 An image-based model of fluid flow through lymph nodes. *Bull. Math. Biol.* **78**, 52–71. (doi:10.1007/s11538-015-0128-y)
54. Cooper LJ, Zeller-Plumhoff B, Clough GF, Ganapathisubramani B, Roose T. 2018 Using high resolution X-ray computed tomography to create an image based model of a lymph node. *J. Theor. Biol.* **449**, 73–82. (doi:10.1016/j.jtbi.2018.04.021)
55. Shanti A, Samara B, Abdullah A, Hallfors N, Accoto D, Sapudom J, Alatoom A, Teo J, Danti S, Stefanini C. 2020 Multi-compartment 3D-cultured organ-on-a-chip: towards a biomimetic lymph node for drug development. *Pharmaceutics* **12**, 464. (doi:10.3390/pharmaceutics12050464)
56. Setukha A, Tretiakova R. 2022 Computational modeling of lymph filtration and absorption in the lymph node by boundary integral equations. *Algorithms* **15**, 388. (doi:10.3390/a15100388)
57. Tretiakova R, Setukha A, Savinkov R, Grebennikov D, Bocharov G. 2021 Mathematical modeling of lymph node drainage function by neural network. *Mathematics* **9**, 3093. (doi:10.3390/math9233093)
58. Giantesio G, Girelli A, Musesti A. 2021 A model of the pulsatile fluid flow in the lymph node. *Mech. Res. Commun.* **116**, 103743. (doi:10.1016/j.mechrescom.2021.103743)
59. Giantesio G, Girelli A, Musesti A. 2022 A mathematical description of the flow in a spherical lymph node. *Bull. Math. Biol.* **84**, 142. (doi:10.1007/s11538-022-01103-6)
60. Bertram CD, Macaskill C, Moore Jr JE. 2018 Contraction of collecting lymphatics: organization of pressure-dependent rate for multiple lymphangions. *Biomech. Model. Mechanobiol.* **17**, 1513–1532. (doi:10.1007/s10237-018-1042-7)
61. Bertram CD, Macaskill C, Moore Jr JE. 2014 Incorporating measured valve properties into a numerical model of a lymphatic vessel. *Comput. Methods Biomech. Biomed. Eng.* **17**, 1519–1534. (doi:10.1080/10255842.2012.753066)
62. Waniewski J. 2006 Mathematical modeling of fluid and solute transport in hemodialysis and peritoneal dialysis. *J. Membr. Sci.* **274**, 24–37. (doi:10.1016/j.memsci.2005.11.038)
63. Formaggia L, Quarteroni A, Veneziani A. 2009 *Cardiovascular mathematics: modeling and simulation of the circulatory system*. Milano, Italy: Springer.
64. Discacciati M, Quarteroni A. 2009 Navier-Stokes/Darcy coupling: modeling, analysis, and numerical approximation. *Rev. Mat. Complut.* **22**, 315–426. (doi:10.5209/rev_REMA.2009.v22.n2.16263)
65. Beavers GS, Joseph DD. 1967 Boundary conditions at a naturally permeable wall. *J. Fluid Mech.* **30**, 197–207. (doi:10.1017/S0022112067001375)
66. Saffman PG. 1971 On the boundary condition at the surface of a porous medium. *Stud. Appl. Math.* **50**, 93–101. (doi:10.1002/sapm197150293)
67. Becker SM. 2017 *Modeling of microscale transport in biological processes*. Cambridge, MA: Elsevier, Academic Press.
68. Penta R, Ambrosi D. 2015 The role of the microvascular tortuosity in tumor transport phenomena. *J. Theor. Biol.* **364**, 80–97. (doi:10.1016/j.jtbi.2014.08.007)
69. Auriault JL, Boutin C, Geindreau C. 2009 *Homogenization of coupled phenomena in heterogenous media*. Paris, France: Wiley.
70. Ochoa-Tapia JA, Whitaker S. 1995 Momentum transfer at the boundary between a porous medium and a homogeneous fluid I. Theoretical development. *Int. J. Heat Mass Transfer* **38**, 2635–2646. (doi:10.1016/0017-9310(94)00346-W)
71. Ochoa-Tapia JA, Whitaker S. 1995 Momentum transfer at the boundary between a porous medium and a homogeneous fluid II. Comparison with experiment. *Int. J. Heat Mass Transfer* **38**, 2647–2655. (doi:10.1016/0017-9310(94)00347-X)
72. Tan H, Pillai KM. 2009 Finite element implementation of stress-jump and stress-continuity conditions at porous-medium, clear-fluid interface. *Comput. Fluids* **38**, 1118–1131. (doi:10.1016/j.compfluid.2008.11.006)
73. Adair TH, Moffatt DS, Paulsen AW, Guyton AC. 1982 Quantitation of changes in lymph protein concentration during lymph node transit. *Am. J. Physiol. Heart Circul. Physiol.* **243**, H351–H359. (doi:10.1152/ajpheart.1982.243.3.H351)
74. Adair TH, Guyton AC. 1983 Modification of lymph by lymph nodes. II. Effect of increased lymph node venous blood pressure. *Am. J. Physiol. Heart Circul. Physiol.* **245**, H616–H622. (doi:10.1152/ajpheart.1983.245.4.H616)
75. Adair TH, Guyton AC. 1985 Modification of lymph by lymph nodes. III. Effect of increased lymph hydrostatic pressure. *Am. J. Physiol. Heart Circul. Physiol.* **249**, H777–H782. (doi:10.1152/ajpheart.1985.249.4.H777)
76. Stohrer M, Boucher Y, Stangassinger M, Jain RK. 2000 Oncotic pressure in solid tumors is elevated. *Cancer Res.* **60**, 4251–4255.
77. Kozeny J. 1927 Ueber kapillare leitung des wassers im boden. *Sitzungsber Akad. Wiss.* **136**, 271–306.
78. Carman PC. 1997 Fluid flow through granular beds. *Chem. Eng. Res. Des.* **75**, S32–S48. (doi:10.1016/S0263-8762(97)80003-2)
79. Chary SR, Jain RK. 1989 Direct measurement of interstitial convection and diffusion of albumin in normal and neoplastic tissues by fluorescence photobleaching. *Proc. Natl Acad. Sci. USA* **86**, 5385–5389. (doi:10.1073/pnas.86.14.538)
80. Tomei AA, Siegert S, Britschgi MR, Luther SA, Swartz MA. 2009 Fluid flow regulates stromal cell organization and CCL21 expression in a tissue-engineered lymph node microenvironment. *J. Immunol.* **183**, 4273–4283. (doi:10.4049/jimmunol.0900835)
81. Dafni H, Israely ZMB, Benjamin LE, Neeman M. 2002 Overexpression of vascular endothelial growth factor 165 drives peritumor interstitial convection and induces lymphatic drain: magnetic resonance imaging, confocal microscopy, and histological tracking of triple-labeled albumin. *Cancer Res.* **62**, 6731–6739. (doi:10.1073/pnas.86.14.538)
82. Bertram CD, Macaskill C, Moore Jr JE. 2014 Development of a model of a multi-lymphangion lymphatic vessel incorporating realistic and measured parameter values. *Biomech. Model. Mechanobiol.* **13**, 401–416. (doi:10.1007/s10237-013-0505-0)
83. Bouta EM, Wood RW, Brown EB, Rahimi H, Ritchlin CT, Schwarz EM. 2014 In vivo quantification of lymph viscosity and pressure in lymphatic vessels and draining lymph nodes of arthritic joints in mice. *J. Physiol.* **592**, 1213–1223. (doi:10.1113/jphysiol.2013.266700)
84. Jäger W, Mikelić A. 2000 On the interface boundary condition of Beavers, Joseph, and Saffman. *SIAM J. Appl. Math.* **60**, 1111–1127. (doi:10.1137/S003613999833678X)
85. Jäger W, Mikelić A. 2009 Modeling effective interface laws for transport phenomena between an unconfined fluid and a porous medium using homogenization. *Transp. Porous Media* **78**, 489–508. (doi:10.1007/s11242-009-9354-9)
86. Auriault JL. 2010 About the Beavers and Joseph boundary condition. *Transp. Porous Media* **83**, 257–266. (doi:10.1007/s11242-009-9435-9)
87. Angot P, Goyeau B, Ochoa-Tapia JA. 2017 Asymptotic modeling of transport phenomena at the interface between a fluid and a porous layer: jump conditions. *Phys. Rev. E* **95**, 063302. (doi:10.1103/PhysRevE.95.063302)
88. Eggenweiler E, Rybak I. 2021 Effective coupling conditions for arbitrary flows in Stokes–Darcy systems. *SIAM Multiscale Model. Simul.* **19**, 731–757. (doi:10.1137/20M1346638)

89. Al Sariri T, Penta R. 2022 Multi-scale modelling of nanoparticle delivery and heat transport in vascularised tumours. *Math. Med. Biol.* **39**, 332–367. (doi:10.1093/imammb/dqac009)
90. Al Sariri T, Simitev RD, Penta R. 2023 Optimal heat transport induced by magnetic nanoparticle delivery in vascularised tumours. *J. Theor. Biol.* **561**, 111372. (doi:10.1016/j.jtbi.2022.111372)
91. Penta R, Merodio J. 2017 Homogenized modeling for vascularized poroelastic materials. *Active Behav. Soft Matter Mechanobiol.* **52**, 3321–3343. (doi:10.1007/s11012-017-0625-1)
92. Mascheroni P, Penta R, Merodio J. 2023 The impact of vascular volume fraction and compressibility of the interstitial matrix on vascularised poroelastic tissues. *Biomech. Model. Mechanobiol.* **22**, 1901–1917. (doi:10.1007/s10237-023-01742-1)